Multi-parameter sensing based on in-line Mach-Zehnder interferometer

by

Yanping Xu

Thesis submitted to the
Faculty of Graduate and Postdoctoral Studies
In partial fulfillment of the requirements for the
M.Sc. degree in Physics

Ottawa-Carleton Institute for Physics
University of Ottawa
Ottawa, Canada

To my family

Abstract

Optical fiber sensors have been intensively studied and successfully employed in various human social activities and daily living, such as industrial production, civil engineering, medicine, transportation, national defense and so on. According to different structures, optical sensors could be divided into various categories. This thesis focuses on studying different kinds of in-line fiber Mach-Zehnder interferometers, which have played an important role among the optical interferometric fiber sensors. The structure composition, fabrication process, physical principle and practical applications of two novel in-line fiber Mach-Zehnder interferometers are proposed and discussed in detail in this work.

The tapered bend-insensitive fiber Mach-Zehnder interferometer (BIF-MZI) is firstly fabricated and used as a fiber vibrometer. The unique double-cladding structure of bend-insensitive fiber not only provides higher mechanical strength to the sensor, but also guarantees a more uniform transmission spectrum， since only a few inner-cladding modes are left interfering with the core mode. A high sensitivity and fast response intensity demodulation scheme is employed by monitoring the power fluctuation of the BIF-MZI at the operation wavelength. Both damped and continuous vibrations are detected using the proposed sensor. It is demonstrated that this sensor responses to an extremely wide range of frequencies from 1 Hz up to 500 kHz with high signal-to-noise ratios (SNRs).

The discrimination of temperature and axial strain is realized based on the dispersion effects of high-order-mode fiber (HOMF) by forming a single mode fiber-high-order-mode fiber-single mode fiber (SMF-HOMF-SMF) structure based in-line Mach-Zehnder interferometer. Unlike some kinds of in-line MZIs such as tapered and core–offset structures

whose cladding modes are excited with different types under changing temperature and strain circumstances, the HOMF is capable of supporting three stable core modes, which guarantees a reliable and repeatable measurements within a large temperature or strain range. A new method based on the fast Fourier transform (FFT) is employed to analyze the mode couplings and their chromatic dispersion and intermodal dispersion properties in HOMF. The strong dispersion effects lead to a multi-peak feature in the spatial frequency spectrum. It is found that peaks that denote the waveform periods at positions that are beyond the critical wavelength possess highly sensitive and distinct phase responses to external disturbances, which provides the possibility to realize the discrimination measurements with high sensitivities and smaller errors by selecting appropriate peaks. The phase demodulation scheme is applied to quantify the temperature and strain changes in terms of phase shifts. Appropriate peak selections according to the practical needs would provide an easy access for applications where more than two parameters are required to be discriminated.

Acknowledgments

I’m so honored to have this opportunity to thank all the people who have helped me over the past two years.

First of all, I would like sincerely thank my supervisors, Professor Xiaoyi Bao and Professor Ping Lu, for their careful guidance and support in my graduate study. It is my great honor to know Prof. Bao and Prof. Lu both at professional and personal level. Prof. Bao, with her strong passion, broad knowledge and thoughtful insight in research, impresses me a lot. Her creative ideas, rigorous attitude and rich research experience have taught and inspired me to challenge the useful but difficult research topics one by one. Prof. Lu provided me not only a lot of insightful and helpful suggestions and ideas during my research process, but also invaluable kind care with my daily lives. His encouragement and constant support greatly increase my confidence in research and contribute to my successful completion of Master studies. I would also express my great gratitude to Prof. Liang Chen for his precious advices and instructive discussions, which significantly improves the quality of this thesis.

Many thanks are given to Dr. Ping Lu for his great ideas, useful suggestions and thoughtful discussions. Dr. Lu has provided much assistance and guidance when I started my research. This thesis cannot be completed without his kind help.

I would like specially thank Dr. Zengguang Qin. He is more than a research partner but one of my sincere friends. His comments and suggestions have greatly benefited me during my research. He was always with me whenever I got confused, lost and disappointed.

I am thankful to my colleagues in Fiber Optics group — Dr. Ganbin Lin, Dr. Wenhai Li, Dr. Xiaozhen Wang, Dr. Dapeng Zhou, Dr. Meng Pang, Mr. Jia Song, Mr. Yang Lu, Mr. Jeremie Harris and Mr. Graeme Niedermayer for their useful technical assistance and discussions.

Finally, I am deeply indebted to my family in China, especially my parents. It is their encouragement, enduring love and understanding for me to pursue my graduate study.

Statement of originality

This work contains no material which has been accepted for the award of any other degree or diploma in any university or other tertiary institution and, to the best of my knowledge and belief, contains no material previously published or written by another person, except where due reference has been made in the text.

I give consent to this copy of my thesis, when deposited in the University Library, being available for loan and photocopying.

SIGNED: ………………………………..

DATE: …………………………………...

Supervisors: Prof. Xiaoyi Bao and Prof. Ping Lu

Contents

List of Figures

List of Tables

List of Acronyms

BIF-MZI	Tapered bend-insensitive fiber Mach-Zehnder interferometer
CD	Chromatic dispersion
CFMZI	Core-offset fiber Mach-Zehnder interferometer
EDFA	Erbium-doped fiber amplifier
FBG	Fiber Bragg grating
FFT	Fast Fourier transform
FLMMZI	Femtosecond laser micromachined Mach-Zehnder interferometer
FP	Fabry-Perot
FSR	Free spectral range
HMZI	Hybrid in-line fiber Mach-Zehnder interferometer
HOMF	High-order-mode fiber
LP	Linearly polarized
LPG	Long period grating
MMF	Multi-mode fiber
MMI	Multi-mode interference
MMZI	Mode-mismatch based Mach-Zehnder interferometer
MZI	Mach-Zehnder interferometer
OPD	Optical path difference
OSA	Optical spectrum analyzer
PCF	Photonic crystal fiber
PZT	Lead zirconate titanate

RI	Refractive index
RIU	Refractive index unit
SEM	Scanning electron microscopy
SMF	Single mode fiber
SMS	Single-mode-multimode-single-mode
SNR	Signal-to-noise ratio
TFMZI	Tapered fiber Mach-Zehnder interferometer
WDM	Wavelength-division multiplexer

Chapter 1

Introduction

This chapter generally reviews the characteristics, advantages, and applications of different types of optical fiber sensors. Discrimination of temperature and strain based on various kinds of optical fiber sensors is recalled. A comparison of vibration detection using optical fiber based vibration sensors over conventional ones is presented. A strong motivation on improving the performance of optical fiber sensors in the above two application areas promotes our recent progress concerning the design, fabrication, practical usage of new-type sensors. The contributions of the proposed fiber sensors would also be discussed in detail.

1.1 Background and motivation

Optical fibers have been widely applied in communication systems, optical sensors, illumination applications, imaging optics and laser gain media since the 1970s when the attenuation in optical fibers was firstly reduced below 20dB/km. Among various potential applications, optical fibers used as sensors show a series of significant advantages and have drawn an intensive attention worldwide. As the optical fiber sensor development gradually matures, the merits of this new technology become evident. An apparent advantage of an optical fiber features its low transmission loss, which guarantees high quality of signal. Optical fiber sensors possess high sensitivities to external physical perturbations such as temperature, strain, acoustic, current, pressure, etc., which surpass other existing techniques usually by tens of or even a hundred decibels. With the immunity to electromagnetic interference and survival to high temperature and corrosive substances, it can be used in various harsh environments. Furthermore, the geometric versatility, small size, and light weight of optical fibers give the unparalleled flexibility in applications with limited space and portable usages. Easy access to low-cost long fibers provides the feasibility of remote and distributed sensing. These advantages have been demonstrated over the past several decades by employing large amount of different types of fiber sensors in various areas.

Optical fiber sensor can be either a point sensor which works at a localized area or a distributed sensor which functions along the entire fiber length. Up to now, the distributed optical fiber sensors are mainly based on optical scattering such as Rayleigh, Brillouin and Raman scatterings. The local external perturbation along the sensing fiber such as temperature, strain, vibration and so on can be detected by the variation in amplitude, frequency, polarization and phase of the backscattering light. However, the distributed sensors suffer the shortcomings such as low sensitivity, high cost, cumbersome system and complicated debugging. Point sensors are a good alternative when distributed measurements are not necessary. Various types of point fiber sensors were proposed and demonstrated based on different kinds of principles and algorithms including fiber Bragg grating, Fabry-Perot interferometer, Mach-Zehnder interferometer and some other novel structures. Compared to the distributed sensors, point sensors have the advantages of high sensitivity, low cost, low weight, easy fabrication and compactness. In some cases, point sensors could be utilized to realize the distributed detection by combining a series of interferometers together, which has been achieved by constructing a merged Sagnac-Michelson interferometer, dual-Sagnac interferometer and so on.

According to different structures, point optical fiber sensors could be divided into several categories, which are listed in the following Table-1.1:

	Sensor type	Sensor structure	Sensor Applications	Ref.
Fabry-Perot fiber sensor	Extrinsic	A SMF as input/output fiber and A MMF as a reflector	Strain	[1]
	Intrinsic	A short air FP near the fiber tip	RI	[2]
		Two internal mirrors inside a SMF	Pressure	[3]
		Femtosecond laser micromachined cavity	Temperature	[4]
Mach-Zehnder interferometer	Two fiber beams	Two fibers form two light beams for MZI	Vibration	[5]
	In-line	Taper, core-offset, laser spot, etc.	Details in Chapter 2	
Michelson interferometer	Two fiber beams	Two fibers form two light beams for Michelson interferometer	Position-distance	[6]
	In-line	Taper, core-offset, etc.	RI,	[7, 8]
Sagnac interferometer		Sagnac loop	Strain, Temperature	[9, 10]
Fiber Grating	FBG	Normal FBG, chirped FBG, tilted FBG	Temperature, strain	[11, 12]
	LPG	Gratings with long periods	Temperature,	[13]

			strain, RI	

Table 1. 1 Various kinds of optical fiber sensors

1.1.1 Temperature and strain sensors:

Temperature and strain are two of the earliest and most widely investigated measurands of optical fiber sensors due to their universality in our daily life. Temperature measurement is vital in enormous practical fields such as multiple industrial segments including temperature monitoring in plant and process engineering, oil and gas production, leakage detection at dikes and dams, as well as recent ecological monitoring, containing groundwater source detection, deep rainforest ambient temperature detection, and underground mine temperature monitoring. Because of the crosstalk induced by ambient fluctuating temperature when conducting strain detection, the discrimination between the two parameters is considered of great concern. The temperature-strain discrimination technique leads to the generation of temperature-insensitive strain sensors and has found its importance in nondestructive detection of civil infrastructure, structure inspection of space industry, and transportation domain. To date, many kinds of fiber sensor structures aiming at simultaneously measuring the two parameters have been designed and applied to practical use, which include fiber Bragg gratings, long period gratings, Sagnac interferometers, fiber Mach-Zehnder interferometers and so on [14-20].

1.1.2 Acoustic/vibration fiber sensors:

Monitoring and inspecting the structure health of aerospace engineering, civil infrastructures as well as environmental protection technology is quite crucial for damage identification, localization and characterization. A high sensitivity and fast responsive device is required to monitor the structural variation under acoustic wave or vibration [21]. Various kinds of fiber based optical sensors including point sensors and distributed ones have been proposed with their unique advantages such as resistance to electromagnetic interference, simplicity and potential low cost over the conventional piezoelectric accelerometers which always suffer from electromagnetic noise. The major kinds of fiber vibrometers are based on interferometric devices, such as Mach-Zehnder (MZ), Michelson, Fabry-Perot, and Sagnac interferometers. Recent proposed point fiber sensor configurations contain a temperature-insensitive vibrometer based on a strain-chirped fiber Bragg grating (FBG) [22], a new type of acoustic sensor based on distributed Bragg reflector fiber laser [23], and a highly sensitive two-beam MZ interferometer with one beam replaced by a single thin gentle fiber taper [5]. Intensity demodulation scheme is extensively utilized to recover the frequency information of the acoustic/vibration event which modulates the phase difference between two interfering signals.

1.1.3 Fiber-optic biosensors:

Fiber-optic biosensors with their high efficiency and accuracy, potential low cost and convenience have been explored to measure various biological species such as cells, proteins, DNA and so on. Relying on the interaction between the samples to be detected and the evanescent field produced by the designed fiber sensor configurations, high sensitivity and selectivity could be achieved not only to respond to low concentrations of analytes, but also to distinguish among the various species. Tapering technique has been verified as an effective way to expose the evanescent field to the milieu as well as increase the penetration depth of the evanescent field [24]. Other effects, such as bending, launching condition of input light, and selected operation wavelength could also influence the strength of the evanescent field. For protein and DNA detection, fluorescence based fiber-optic biosensors have been widely employed at low level of molecular concentrations [25, 26]. It has the advantage of high selectivity among species, however, multiple steps to prepare the samples and sensor increase the complexity of the detection and the shortage of sensitivity. Surface plasma resonance based fiber-optic biosensors have recently been developed to the most commonly used devices [27, 28].

1.1.4 Magnetic field/current sensors:

In recent years, optical fibers have been used in the area of electromagnetic field measurement as magnetometers and current sensing which have been playing an important role in supervision and control of large-scale circuit system and current monitoring scheme. According to different physical principles, current fiber sensors could be categorized into two classes, one is based on the Faraday effect [29-34] and the other one is based on the thermal effect [35, 36]. The former kind relies on the inherent property of silica in terms of its Verdet constant. The rotation of polarization of the input light is proportional to the intensity of the applied magnetic field which is induced by the surrounding current. The Faraday rotation angle of the polarization is expressed as a function of the Verdet constant, magnitude of the magnetic field and the interacting length. Apparently, this performance of the method is limited by the term of the Verdet constant. The latter one is based on the thermal effect of the current. When a current passes through the metal-coated optical fiber, the Ohm’s heat induces a phase change of the guided light within the fiber. This method needs only a short length of fiber but usually requires complex fabrication process due to a requirement of adding metal layer onto the fiber surface.

1.1.5 Other types of sensors:

Other types of optical fiber sensors aiming at detection of chemical species in liquid/gas, bending sensing and displacement quantification have already been proposed and put into use. The detection of chemical composition in the gas and vapor phase is crucial in industry, environment and medical care. Two kinds of fiber Mach-Zehnder interferometers with different fabrication approaches are designed for refractive indices measurements of liquid and gas, respectively [37, 38]. By exposing one light beam into the medium which is composed of the unknown chemical species, the resonance wavelength position in the transmission spectrum is modulated by the changed optical path length difference between the two light beams. These compact all-fiber based devices achieve high refractive index sensitivity and are suitable for application in a wide range of areas.

Bending sensor is an important device in the areas of composite material structures and smart systems. Long period gratings (LPG) are firstly utilized as the bending sensor based on the wavelength shift in the transmission spectrum or mode splitting [39, 40]. The Sagnac loop mirror based fiber bending sensor [41] which uses light intensity modulation principle is also presented to overcome the poor stability of macro-bend sensor [42, 43]. However, the shortage of low bending sensitivity of Sagnac loop sensor soon gives way to the Mach-Zehnder interferometer based bending sensor [44, 45] with a higher bending sensitivity. For displacement sensing, it has been employed to improve the functionality and raise the quality of products by means of position monitoring and controlling in the industrial machines.

Linear variable displacement transducer is a typical example of sensor for measuring displacement. Owing to utilizing the contact means to fulfill the test, they often could not be practically applied when the contact is not desired or feasible. Instead, fiber-optic devices, with noninvasive sensing techniques, have succeeded in improving the degree of measurement integrity, simplicity and cost-effective features [46]. Relating the wavelength shift in the interference spectrum with the displacement variation provides the availability for FBG based [47] and Michelson interferometer [48] based fiber sensor for displacement sensing. Provided that it is calibrated appropriately, the magnitude of displacement could be quantified proportionally to the wavelength shift value.

1.2 Thesis contribution

In this thesis, two novel configurations of in-line fiber Mach-Zehnder interferometers are proposed for static and dynamic sensing, respectively. The phase-modulation scheme and intensity-modulation scheme are separately employed in simultaneous measurement of temperature and strain and detection of damped and continuous vibration. These parameters are accurately detected with high sensitivity and small errors, which demonstrates that the proposed sensors would be a worthy choice for potential commercial applications.

Firstly, we propose the tapered bend-insensitive fiber Mach-Zehnder interferometer (BIF-MZI) for damped and continuous vibration sensing. This is the first time that an in-line fiber Mach-Zehnder interferometer is utilized as a vibration sensor. Though the most conventional piezoelectric accelerometer is widely used in industries, they have some drawbacks of easily being disturbed by surrounding electromagnetic interference, cumbersome size and weight and so on. Vibration detection based on all-fiber based sensors, for example, fiber Bragg grating, Fabry-Perot interferometer and two-beam fiber Mach-Zehnder interferometer are also investigated. However, these sensors suffered from high cost, complicated packaging and fabrication and low degree of integrity. The in-line Mach-Zehnder structure is a good alternative to overcome the above drawbacks. Besides the unparalleled advantages the in-line structure owns, the bend-insensitive fiber chosen in the proposed device exhibits unique merits. Traditional tapered in-line MZI usually needs the removal of the protective jacket along the central fiber between the two tapers in order to avoid the excited cladding modes suffering from high attenuation loss. This is not an issue and even helpful when measuring temperature and refractive index which requires the fiber cladding fully immersed in the environment to be measured. However, removing the jacket of the fiber decreases the mechanical strength of the device and the sensor is difficult to be applied in vibration measurement where the contact would introduce disturbance to the interference pattern and cause nonlinearity in results of intensity demodulation method. The bend-insensitive fiber possesses double layers of claddings which are separated by a ring of air holes. Keeping the coating along the device will cause the outer-cladding modes depletion, while the inner-cladding modes still remain to interfere with the core mode.

A time domain intensity-modulated signal is obtained using the proposed device by monitoring the intensity change at a specific operation wavelength under vibration. This method requires the fringes in the transmission spectrum to be uniform and distinct. We’ve selected the appropriate taper size to make sure only two dominant inner-cladding modes are excited and kept propagating along the device to guarantee the uniformity of interference fringes as well as a distinct contrast of the spectrum. The proposed device with this mode number controllable feature prevails over the tapered single mode fiber MZI in which case usually a series of cladding modes would be observed. Based on the fast response intensity demodulation scheme, the proposed sensor realizes a very broad range of frequency measurements from several Hertz to hundreds of kilo-Hertz with high signal-to-noise ratio.

Secondly, we propose a new technique based on chromatic dispersion effects of a high-order-mode fiber (HOMF) to discriminate temperature and axial strain. This is realized by sandwiching a piece of HOMF with two standard single mode fibers to form a SMF-HOMF-SMF Mach-Zehnder interferometer. A phase demodulation scheme is performed to quantify the measurands in terms of phase shift of the selected mode coupling peaks in the spatial frequency domain. In previous work, the static sensing is commonly accomplished by monitoring the peak wavelength position shift in the transmission spectrum of the sensor. Although this approach owns the merit of simplicity, it has difficulty in exactly determining the peak position. This is due to the superposition of multiple interferences caused by multiple coupling modes existing inside the sensor. Since each interference signal would lead to different peak profile in the transmission spectrum and each of them responses differently to temperature or strain, the peak wavelength is hard to be determined by usual peak profile fitting method. The proposed scheme shows significant advantages over previous method with every pair of coupling modes discriminated and the ability to achieve multi-parameter measurements.

The HOMF supports three stable core modes. The unique waveguide structure of HOMF introduces strong chromatic dispersion (CD) effects to these supported modes. The interference patterns resulted from coupling among the three core modes will be intensely modulated by the CD effects, which leads to a large amount of coupling peaks in the spatial frequency domain. We have demonstrated that the phase responses of different peaks have different temperature and strain dependences. The multi-peak feature in the spatial frequency domain provides abundant choices of sensitivities to the environmental disturbances, which makes the proposed device potentially applicable in situations where more than two parameters are required to be discriminated.

1.3 Thesis outline

This thesis contains five chapters and is organized as follows:

Chapter 2 lists several major kinds of in-line Mach-Zehnder interferometers. Interferometer structures, fabrication processes, working principles and applications of these devices are described. Some representative previous works are also presented as examples in this part.

Chapter 3 proposes a tapered bend-insensitive fiber Mach-Zehnder interferometer for damped and continuous vibration sensing. The fabrication procedure, operation principle and experimental setups are introduced and a wide range of frequency measurement results and analysis are given.

Chapter 4 studies the dispersion effects of high-order-mode fibers on temperature and axial strain discrimination. Simulation results of the chromatic dispersion effects of the supported modes in high-order-mode fiber are presented and then experiments on simultaneous temperature and strain measurement based on dispersion effects are described and discussed.

Chapter 5 concludes all the work in this thesis and proposes possible directions for future research.

Chapter 2

In-line fiber Mach-Zehnder interferometer

This chapter focuses on reviewing several typical kinds of in-line fiber Mach-Zehnder interferometers from the recent literature. These include: Tapered fiber Mach-Zehnder interferometer (section 2.2), Mode-mismatch based Mach-Zehnder interferometer (section 2.3), Core-offset fiber Mach-Zehnder interferometer (section 2.4), Grating based Mach-Zehnder interferometer (section 2.5), Laser micromachined Mach-Zehnder interferometer (section 2.6), Hybrid in-line Mach-Zehnder interferometer (section 2.7). Summary of the state of art in-line fiber Mach-Zehnder interferometer is presented in section 2.8. With great advantages of compact structure and easy manufacturing features, this type of interferometer has been widely studied and become a hot topic in the fiber optics area. The fabrication process, composition and structure, operation principle and published applications for each kind are addressed in detail.

2.1 Introduction

Fiber Mach-Zehnder interferometers have been one of the oldest and most important optical fiber instruments. A typical conventional fiber Mach-Zehnder interferometer consists of two fiber beams which are split and combined by two optical couplers. The first coupler splits the incident light into two fiber beams. Usually the lengths of the two fiber beams are controlled to be different to introduce optical path difference (OPD) between the two light paths. At the second coupler an interference spectrum is obtained as the two beams combine together with a certain OPD. The conventional two-beam fiber MZIs have been widely employed as optical filters, fiber modulators, environmental sensors. However, these two-beam fiber MZIs have their own limitations, such as complicated structure, big size and high cost. To overcome the above drawbacks, an in-line fiber MZI based on core-cladding-mode coupling has been proposed recently. Two light arms are both inside the same fiber in terms of core mode and cladding modes. The cladding modes which have energy distributed in both core and cladding regions are excited by particular light steering elements, i.e. taper, core-offset, mode-mismatch, etc. Using only one piece of fiber, the in-line structure provides several advantages over conventional one such as compactness, high integrity, light weight, low cost and high stability.

To investigate how light propagates along the fiber in the form of core mode and cladding modes, the wave equation is needed for analysis. A regular optical fiber is normally a weakly coupled waveguide which supports light modes propagating along the fiber in terms of linearly polarized modes ($LP_{\upsilon m}$). The propagation constants for LP modes are obtained by accurately solving a set of scalar wave equations. The electric fields that propagate in the z-direction along the fiber satisfy the scalar wave equation, which is given by:

$$(\frac{\partial^2}{\partial r^2}+\frac{1}{r}\frac{\partial}{\partial r}+\frac{1}{r^2}\frac{\partial^2}{\partial \phi^2}+k^2n^2-\beta^2)\psi=0 \tag{0.1}$$

where ψ represents the electric or magnetic field, k is the free space wavenumber, n is the refractive index and β is the propagation constant with the expression $\beta=kn_{eff}$.

The effective refractive index of core mode n_{eff} satisfies $n_{\mathrm{cl}} < n_{\mathrm{eff}} < n_{\mathrm{co}}$, we consider the bounded solution with core-cladding interface. The solution of Equation 2.1 is given as

$$\psi=\begin{cases} AJ_{\upsilon}(u_1 r)e^{i\upsilon\phi} & if\ 0\le r\le\rho \\ CK_{\upsilon}(\omega r)e^{i\upsilon\phi} & if\ \rho\le r\le\rho_{cl} \end{cases} \tag{0.2}$$

where u_1 and ω are defined as

$$u_1=k(n_{co}^2-n_{eff}^2)^{\frac{1}{2}} \tag{0.3}$$

$$\omega=k(n_{eff}^2-n_{cl}^2)^{\frac{1}{2}} \tag{0.4}$$

A and C are constants, ρ and ρ_{cl} are core and cladding radii, respectively. J_{υ} and K_{υ} are the υ_{th} order Bessel function of the first kind and the modified Bessel function of the second kind, respectively. Continuity of electromagnetic field ψ and its first derivative at the core boundary r=ρ relates the values of A and C and leads to a set of eigenvalue equations as [49]

$$u_1\frac{J_{\upsilon+1}(u_1\rho)}{J_{\upsilon}(u_1\rho)}=\omega\frac{K_{\upsilon+1}(\omega\rho)}{K_{\upsilon}(\omega\rho)} \tag{0.5}$$

The eigenvalues obtained from Equation 2.5 are the core modes $\mathrm{LP}_{0\mathrm{m}}$.

The effective refractive index of cladding mode n_{eff} satisfies $n_{air} < n_{eff} < n_{cl}$, we consider the bounded solutions with the core-cladding and cladding-air interfaces. The solution of Equation 2.1 is solved based on a three-layer step-index fiber model [50] with dispersion relation, which is given as

$$\psi = \begin{cases} AJ_\upsilon(u_1 r)e^{i\upsilon\phi} & if\ 0 \le r \le \rho \\ [BJ_\upsilon(u_1 r) + CY_\upsilon(u_2\rho)]e^{i\upsilon\phi} & if\ \rho \le r \le \rho_{cl} \\ DK_\upsilon(\omega_3 r)e^{i\upsilon\phi} & if\ r \ge \rho_{cl} \end{cases} \tag{0.6}$$

where the modal parameters are defined as

$$u_2 = k(n_{cl}^2 - n_{eff}^2)^{\frac{1}{2}} \tag{0.7}$$

$$\omega_3 = k(n_{eff}^2 - n_{air}^2)^{\frac{1}{2}} \tag{0.8}$$

A, B, C and D are constants, Y_υ is the υ_{th} order Bessel function of the second kind. Similar to the core mode, the continuity of electromagnetic fields and their derivatives at the two interfaces results in a set of equations relating the values of A, B, C and D and provides the eigenvalue equations from consistency conditions. The calculated eigenvalues are the cladding modes $\text{LP}_{\upsilon m}$ (υ>0).

The mode field patterns of excited cladding modes in in-line fiber Mach-Zehnder interferometers are determined by the azimuthal symmetry of the light steering elements. If they are axisymmetric, only the modes with the same azimuthal symmetry ($\text{LP}_{0\text{m}}$) could be excited. The LP_{02} mode usually dominates among the excited symmetric modes. While in the non-axisymmetric case, the energy of the fundamental mode LP_{01} will mostly be coupled to the non-axisymmetric mode with closest effective refractive index, i.e. the LP_{11} mode. A coupling coefficient η is induced to characterize energy conversion from the LP_{01} mode to high-order modes and it is generally given as:

$$\eta = \frac{\left| \iint \psi_{01}(x,y)\psi_{\upsilon\text{m}}^*(x,y)dxdy \right|^2}{\iint \psi_{01}\psi_{01}^* dxdy \iint \psi_{\upsilon\text{m}}\psi_{\upsilon\text{m}}^* dxdy} \tag{0.9}$$

where ψ_{01} is the electromagnetic field of LP_{01}, $\psi_{\upsilon m}$ are the electromagnetic fields of cladding modes.

2.2 Tapered fiber Mach-Zehnder interferometer

Tapering is an effective technique to couple a relative large ratio of energy in the fundamental mode to high-order cladding modes in optical fiber. A tapered fiber Mach-Zehnder interferometer (TFMZI) is a very important fiber device which has found applications as optical sensors, power couplers, multiplexers, and so on. As light propagates along the tapered fiber region where the diameter of optical fiber is decreased to tens of micrometers or even several micrometers, the energy field distribution of the fundamental mode is unable to vary rapidly enough to keep up with the local fundamental mode whose field distribution is determined by the local taper cross-sectional profile. As a result, the energy loss of the original fundamental mode would be converted to high-order cladding modes. This is also called a core-cladding transition. The transition value, $V_{core/cladding}$, is expressed as [51]

$$V_{\mathrm{core}/cladding} = \frac{2\pi}{\lambda}\frac{d}{2S}\sqrt{n_{core}^2 - n_{cladding}^2} \approx \sqrt{\frac{2}{\ln S}}(1+\frac{0.26}{lnS})^{-1/2} \qquad (0.10)$$

where d is the diameter of the fiber taper and S is the diameter ratio of core to cladding. According to the taper angle, fiber tapers are generally categorized into two types: an adiabatic or gentle taper and a nonadiabatic or abrupt taper. During the fabrication process, the fiber diameter is decreased by heating and pulling the two fiber ends. The gentle taper is usually heated by a gas flame and stretched by programmed translation stages. The slow stretching technique guarantees small taper angles in the down-taper and up-taper regions as well as a uniform waist region. Compared with the gentle taper, an abrupt taper is commonly manufactured by electrical arc method using built-in fiber tapering programs in a fusion splicer. This kind of taper has a steep slope and its taper waist size is controlled by the magnitude of electrical arc and stretching time and speed. Figure 2.1 gives a typical image profile of an abrupt taper.

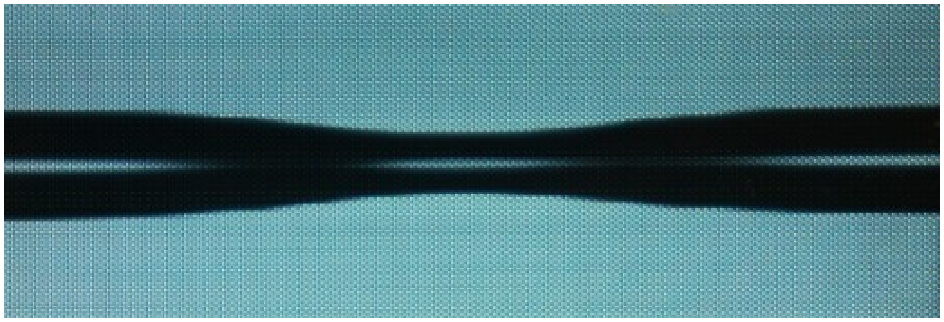

Figure 2.1 Image profile of an abrupt taper.

The tapered fiber Mach-Zehnder interferometer is usually constructed by concatenating two abrupt tapers as shown in Figure 2.2. The two tapers act as two light steering elements to couple light to high-order modes and back to the fundamental mode. When the input light passes through the first taper, part of the energy would be coupled into high-order modes because of the steep slope of the taper. In principle, the steeper the slope, the more energy will be coupled to high-order modes as well as a larger number of modes will be excited. At the second taper, high-order modes are coupled back to the fundamental mode and the output interference signal is a result of multi-modes coupling. The taper size determines the contrast and uniformity of the interference fringes, and the separation distance between the two tapers controls the free spectral range (FSR) of the output signal.

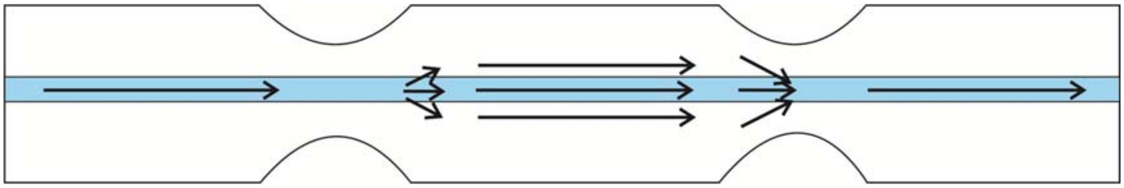

Figure 2.2 Profile of tapered fiber Mach-Zehnder interferometer.

Since TFMZIs have very high sensitivities to external disturbances, various sensing applications have been realized using this structure, such as temperature, strain, refractive index, liquid level, lateral stress, multi-parameter discrimination measurement, and so on. In [52], a TFMZI utilized as a strain sensor was presented. Two abrupt tapers were made along a standard single-mode fiber. The applied strain elongated the length of the sensor as well as changed the waveguide structure of the fiber, which led to the change of the effective refractive index of each mode, therefore the optical path difference between the coupling modes were changed and observed as fringes shift in transmission spectrum. The transmission spectra under different axial strains were recorded by an optical spectrum analyzer (OSA). By monitoring the resonance wavelength shift as a function of the applied strain, the response of the sensor to different strain could be obtained. In this work, a high sensitivity of 2000 nm/ε was achieved.

The temperature and refractive index were also successfully discriminated by using TFMZI [53]. The sensor was put into a water bath which could change and maintain the surrounding temperature. KCl solutions with different concentrations were used to change the refractive index around the sensor. Since the Germanium-doped core had a higher response than that of the pure silica cladding, the refractive indices changes in the core and cladding regions were different under the same temperature changes. The solution around the sensor had little influence on the energy distribution in the core region, but made a large difference in that of the cladding region. Therefore both the temperature and the surrounding solution changed the coupling conditions in the sensor and gave rise tofringe shifts. Wavelength shift method was also employed in this work. Since it was demonstrated that different interference orders in the transmission spectrum owned different wavelength shift response to temperature and refractive index, the discrimination of the two parameters was realized by selecting two different peak wavelengths and monitoring their responses to the environmental change. Finally, a character matrix was found to represent the sensing performance of the TFMZI.

Other applications using TFMZIs include liquid level and lateral stress sensing. In liquid level sensing [54], the TFMZI was vertically inserted into the liquid to be measured. The transmission spectra were recorded with an increasing liquid level in step. As the level rose up, the effective RI of cladding modes were increased accordingly. The difference between the RIs of the core mode and cladding modes kept decreasing, which led to the blue-shift in the transmission spectrum. The lateral stress sensing was conducted by applying a transverse pressure using a microscope slide on the center of the TFMZI [55]. The transmission spectra of the TFMZI were recorded under different lateral stress conditions at different loading positions along the interferometer length and a FFT algorithm was performed upon the transmission spectra to obtain spatial frequency spectra. The amplitude and spatial frequency of different peaks in the spatial frequency domain corresponding to different cladding modes were effectively utilized to evaluate the deformation of local fiber geometry.

2.3 Mode-mismatch based Mach-Zehnder interferometer

A mode-mismatch based Mach-Zehnder interferometer (MMZI) utilizing multimode interference (MMI) in single-mode-multimode-single-mode (SMS) fiber structure has been intensively investigated and widely employed in beam splitters, combiners and multiplexers for optical communications. SMS based MMZI has been used as various optical devices, such as a fiber lens, a displacement sensor, a refractometer sensor, and so on.

Figure 2.3 A typical structure of Mode-mismatch based Mach-Zehnder interferometer

A typical SMS structure is fabricated by splicing two pieces of standard single-mode fibers to the two ends of multimode fiber without offset as shown in Figure 2.3. The multimode fiber has a step-index profile but with a much larger size of the core region compared with the SMF. The input light is launched into the lead-in SMF and propagates in the form of the fundamental core mode. Since the core size of SMF is much smaller than that of MMF which is usually capable to support multiple core modes, the difference in the mode field diameters between the fundamental core modes of the SMF and MMF leads to the decomposition of the fundamental core mode from the SMF and excitation of the first few modes supported in the MMF. Given that the fibers are axially aligned at the first splice, only the circular symmetric eigenmodes i.e. the LP_{0m} modes are excited [56]. At the second splice point, the relative phase differences between various modes of the MMF determine the energy coupled from these modes to the lead-out SMF. Mathematically, if the field distribution of the input light is denoted as $E(r,0)$ and the field profiles of LP_{0m} as $F_m(r)$, the energy of input light can be expressed as the sum of all the excited eigenmodes in the MMF:

$$E(r,0)=\sum_{m=1}^{M} c_m F_m(r) \tag{0.11}$$

with the excitation coefficients of each mode in MMF given by:

$$c_m=\frac{\int_0^\infty E(r,0)F_m(r)rdr}{\int_0^\infty F_m(r)F_m(r)rdr} \tag{0.12}$$

Much attention has been paid on the temperature and strain sensitivity when SMS based MMZIs are utilized as sensors. The refractive index profile, dopant species and concentrations all contribute to different responses to temperature/strain in the transmission spectrum. It has been demonstrated that the SMS structures using parabolic index MMF and step-index MMF have different spectral dependence on increasing temperature or strain, where the former kind exhibits a red spectral shift and the latter one a blue spectral shift [57]. Generally, there exists a critical wavelength in the transmission spectrum of a SMS based MMZI. The meaning of the critical wavelength has been theoretically verified as a position at which the curve of the phase difference between the two dominant modes ($\Phi=(\beta_1-\beta_2)L$) as a function of wavelength has a zero slope. Usually when the temperature or strain increases, the critical wavelength does not show any significant spectral shift, while the wavelength shorter or longer than the critical wavelength would have opposite responses to the two parameter changes. [57] reported the responses of a MMF with different types of dopants in the core region. The Ge-doped MMF showed a critical wavelength around 0.925 μm on lower and higher sides of which the spectrum gave a red-shift and a blue-shift, respectively.

However, no critical wavelength was found for the P-doped MMF within the same wavelength range which indicates that changing the type of dopant would change the critical wavelength. Besides, the doping concentration was another important factor that can adjust the critical wavelength and had the potential to be controlled for appropriate critical wavelength selection for temperature and strain sensing.

Another kind of MMZI is based on a high-order-mode fiber (HOMF). Similar to the MMF, a HOMF has a relatively larger core size than that of the standard single-mode fiber. While it differs from MMF in that the core region of HOMF consists of several layers with different refractive indices. A typical HOMF based MMZI example is proposed in [58]. The HOMF utilized here had a core composed with five distinct layers. The transmission spectrum of this structure also showed a critical wavelength feature. Peaks near the critical wavelength were found to have a higher sensitivity to temperature and strain. It was demonstrated that the intensity at the critical wavelength can be monitored to quantify the parameter changes. Simulations were carried out to investigate the chromatic dispersion effect on each guided mode in the HOMF and the recovery transmission spectrum had a very high similarity with the experimental one, which verified two circularly symmetric core modes i.e. the LP_{01} and LP_{02} modes were dominantly coupling pair inside the structure.

2.4 Core-offset fiber Mach-Zehnder interferometer

Core-offset structure has been widely utilized as an optical attenuator in optical communication systems for wavelength balancing, input power control and power equalization in wavelength division multiplexing systems. This structure is realized by fusion splicing two pieces of fibers with a pre-set offset value i.e. usually several micrometers.

Core-offset fiber Mach-Zehnder interferometer (CFMZI) is made up of two such core-offset splicing points. When the input light is launched into the lead-in fiber in the form of the fundamental core mode, it will split into two paths, with one fraction of light coupled to the cladding in the form of cladding modes and the remaining light still in the core region. To prevent the cladding modes from suffering high attenuation loss, the coating along the second fiber must be stripped. At the second offset splicing point, the cladding modes couple back to the core mode and an interference signal is observed at the lead-out fiber end due to the phase difference between them. A schematic profile of the core-offset fiber Mach-Zehnder interferometer is presented in Figure 2.4.

Figure 2.4 A schematic profile of core-offset fiber Mach-Zehnder interferometer

A CFMZI using a standard single-mode fiber was firstly proposed in [8]. Three pieces of single-mode fibers were fusion spliced with a core-offset value. The coating along the central fiber was removed. It was found that the relative offset directions between the two offset splicing points greatly influenced the output interference performance. This was investigated by making one offset splicing point in one end of the bare fiber and the other end was aligned with different offset directions to another piece of fiber. As a result, the contrasts of the resultant transmission spectra differed a lot from each other. It was indicated that selecting an appropriate relative offset direction was very crucial to improve the sensor performance.

CFMZIs based on other types of fibers are also realized. An all-fiber photonic crystal fiber (PCF) based CFMZI was manufactured by fusion splicing three pieces of PCFs with a lateral offset [59]. Experiments showed that only one cladding mode was excited in the central PCF, which was demonstrated by the existence of only one peak in the spatial frequency spectrum. The spatial frequency of the transmission spectrum was linearly proportional to both the length of the interferometer and the effective refractive index difference between the fundamental core mode and the excited cladding modes. This interferometer has the capability for temperature and strain sensing by monitoring the wavelength spectrum shift. Another CFMZI consisting of a central hollow core fiber sandwiched by two single-mode fibers was shown in [60]. By splicing the single-mode fiber and the hollow core fiber with a core-offset, the incident light was separated and propagat in two paths of the air core region and the solid core region. Due to the large refractive index difference between the air core mode and cladding modes, the length of the central fiber was controlled to a short value i.e. 1 mm to make sure fringes could be distinguished more clearly within the operation wavelength range. This miniature MZI was successfully utilized for temperature and strain sensing with high sensitivities.

2.5 Grating based Mach-Zehnder interferometer

Fiber gratings are in-fiber devices which have found many applications in spectral filters, dispersion compensating components, wavelength multiplexing systems, fiber modulators, environmental sensors, and so on. They can be inscribed on optical fibers using either holographic or non-holographic methods. By periodically modifying the refractive index of the fiber core region with different periods, the fiber gratings are generally categorized into two classifications: short-period fiber gratings i.e. fiber Bragg gratings (FBG) with sub-micron period and long period grating (LPG) with a period ranging from 100 μm to 1 mm. A FBG couples the input light to the counter-propagating mode while LPG couples light to the co-propagating mode. With the co-propagating excitation property, a LPG has acted a very important role in an interferometer sensor when two LPGs are combined as a pair to form a LPG based Mach-Zehnder interferometer (LPGMZI).

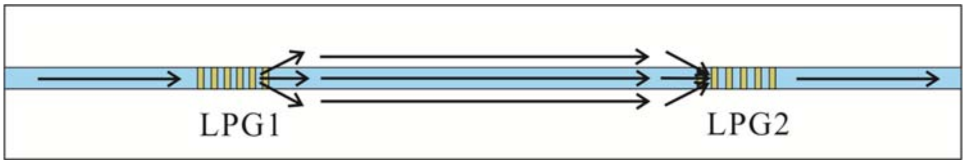

Figure 2.5 LPG based Mach-Zehnder interferometer (LPGMZI)

The structure of a LPGMZI is shown in Figure 2.5. An LPG basically couples the input light originally confined in the fundamental core mode to co-propagating cladding modes which satisfy the phase matching condition expressed by [61]

$$\lambda = [n_{core}(\lambda) - n^{i}_{cladding}(\lambda)]\Lambda \qquad (0.13)$$

Where $n_{core}(\lambda)$ is the effective refractive index of the fundamental core mode and $n^{i}_{cladding}(\lambda)$ is the effective refractive index of the *i*th cladding mode, Λ is the modification period of the LPG.

Once the cladding modes are excited, both the cladding modes and the core mode can propagate along the fiber as long as the coating along the fiber between the two LPGs is removed,. The relative phase difference between the core mode and cladding modes is given by [62]

$$\Psi = \Phi_{in}(\lambda, d) - [\beta_{core}(\lambda) - \beta^{i}_{cladding}(\lambda)](L-d) \tag{0.14}$$

where $\Phi_{in}(\lambda, d)$ is the sum of the phase shifts induced in both LPGs, d is the length of grating, and L is the center-to-center separation between the two LPGs, $\beta_{core}(\lambda)$ and $\beta^{i}_{cladding}(\lambda)$ are the propagation constants for each mode. At the second LPG, cladding modes are coupled back to core mode, which lead to an interference transmission spectrum observed at the output port. In the case that the length of the LPG compared to the separation of the two LPGs can be ignored, the free spectral range is given by

$$\text{FSR}=\frac{\lambda^2}{\Delta \text{m} L} \tag{0.15}$$

where the *Δm* is the effective group index difference between the core mode and each excited cladding mode. In [62], it was also demonstrated that when the LPG length was comparable with the separation, the FSR of a transmission spectrum was dominantly influenced by the phase shift induced within the LPG region. A work based on such a small separation distance was published [63]. A LPG pair was fabricated with a small separation of 2 mm and utilized as a temperature sensor. This small separation improved the sensor in the sharpness of the transmission spectrum and the measurement resolution as well as temperature variation measured within a much shorter length range.

LPGMZI also owns a high sensitivity to the external refractive index variations. High refractive index measurement using LPGMZI is proposed in [64]. Surrounded by solutions with a refractive index value larger than that of the silica, the device showed higher intensity sensitivity over the single LPG sensor. A leaky configuration model was established and then validated by experimental results. The thermo-optic coefficients of the fiber core material were obtained by using a LPGMZI [65]. The peaks of the transmission fringes were measured to determine the refractive index difference between the core and cladding modes. The refractive index of the fiber core was obtained in terms of wavelength. Fiber cores with Germanium doped and boron co-doped were measured with thermo-optic coefficients of $1.1\times10^{-5}\,/^{o}\,C$ and $0.75\times10^{-5}\,/^{o}\,C$, respectively. To enhance the sensitivity of the LPGMZI, a taper as seeded between the two LPGs to improve the refractive index measurements [66]. The experimental results showed a significant increase in sensitivity which was about five times higher than that of a normal LPG pair. Besides a single-mode fiber based LPGMZI, this kind of interferometer was also achieved using a photonic crystal fiber [67].

2.6 Laser micromachined Mach-Zehnder interferometer

Laser micromachined Mach-Zehnder interferometers mainly include two types: a femtosecond laser based MZI and a CO_2 laser based MZI. With recent advancements in the ultrafast pulse laser technology, new fabrication method for nano-fiber structures is employed. The laser beam can be focused on a target material and create optical features at the focal point. Compared to other fabrication methods, the femtosecond laser based technique possesses a unique ability of 3-D microstructure fabrication.

The influence of femtosecond laser modification upon the material can be divided into destructive and nondestructive according to the power magnitude utilized. Nondestructive fabrication means the power of the laser is below the ablation threshold of the material and the modification result shows a changed refractive index profile of the material by the laser source. This effect has found applications in optical waveguides, gratings, and directional couplers [68-70], etc. On the contrary, the destructive fabrication uses a power higher than the ablation threshold of the target material, which can directly sculpture the material into desired structures. This method has been utilized for manufacturing optical devices such as microlenses, microfluidic channels, fiber in-line Fabry-Perot interferometers, and optical switches [4, 71-73].

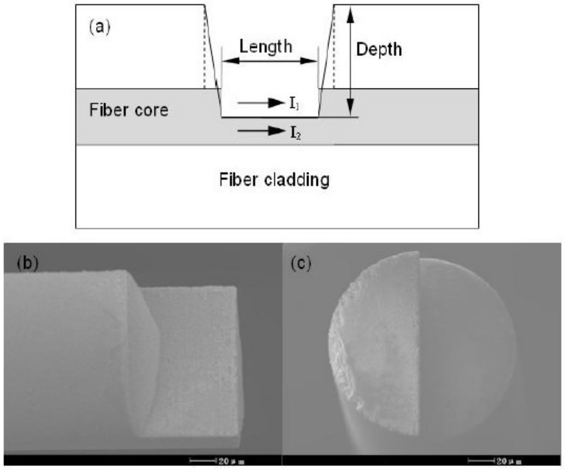

Figure 2.6 Femtosecond laser micromachined Mach-Zehnder interferometer. (a) Schematic illustration. (b) Side view (a half part). (c) Cross section. [74]

A femtosecond laser micromachined Mach-Zehnder interferometer (FLMMZI) was fulfilled by side-ablating a U-shape microcavity in a standard single-mode fiber [37]. The cladding region and partial core region were removed by the laserwhich is shown in Figure. 2.6. The total ablation depth was about a half diameter of the fiber, which approximately removed half of the fiber core. When incident light passed through the ablation region, the light was split into two paths. One was still propagating inside the core, the other was transmitting through the air cavity. The refractive index difference between the air and the fiber core induced the optical path length difference between the two light beams. As a result, the output signal gave an interference pattern which was modulated by the length of the microcavity. The fabrication process of the FLMMZI was presented in and applications for temperature and refractive index measurements were performed [74]. It was found that the transmission spectra changed with the femtosecond laser ablation parameters. The longer the trench length was controlled, the shorter the free spectral range would be. This interferometer was successfully employed in refractive index and temperature sensing. For both low and high refractive index sensing, it showed an extreme high sensitivity up to 10^4 nm/RIU [37].

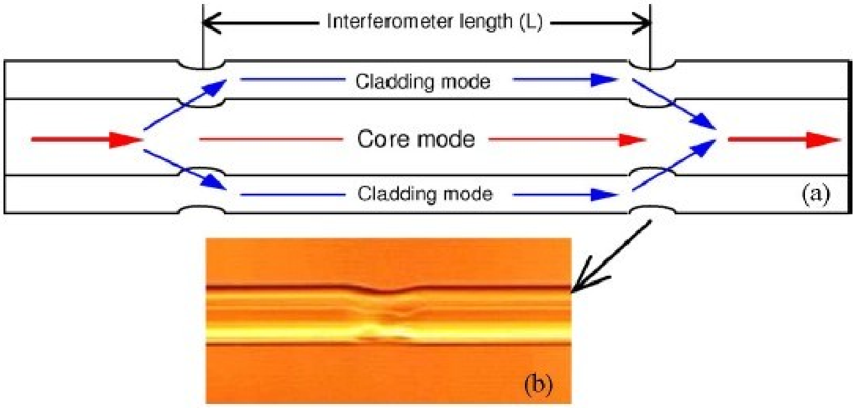

Figure 2.7 CO2 laser micromachined Mach-Zehnder interferometer. (a) Schematic illustration. (b) Microscopic image of the laser modification region. [75]

The CO_2 laser has been previously used as a heat source for modifying optical fibers as devices such as scanning near-field microscope tips, long period fiber gratings, microcouplers, microtapers, and so on. A CO_2 laser micromachined MZI was firstly proposed in [75]. In this work, two modification points (see Figure 2.7) along a single mode fiber were made by a CO_2 laser based on its irradiation effect. The modification induced two microbends on the fiber, which took on a similar role as the two tapers in the tapered fiber Mach-Zehnder interferometer. One microbend was responsible for exciting cladding modes and the other one was for coupling cladding modes back to core mode. An apparent interference fringes were obtained at the transmission spectrum. Several sample interferometers were fabricated and tested as a temperature and refractive index sensor. The experimental results showed that the sensor's sensitivity to refractive index variation was slightly smaller than that of a LPG sensor, which is probably due to the low-order cladding modes excited by the CO_2 laser.

2.7 Hybrid in-line fiber Mach-Zehnder interferometer

The above mentioned microstructures such as the taper, core-offset, mode mismatch, LPG, and laser irradiated spot are not only capable of forming an in-line fiber Mach-Zehnder interferometer with the corresponding pair of themselves, but also can be utilized to form a hybrid in-line fiber MZI (HMZI) by choosing and combining two of them. These hybrid structure based interferometers are designed and fabricated for purposes of either enhanced sensitivity to external perturbation or cost-effectiveness and easy fabrication according to different practical needs. These new designed optical devices have been widely used as a curvature sensor, an inclinometer, a temperature and axial strain sensor, an optical filter, and a wavelength-division multiplexer (WDM). So far, various HMZIs combining different microstructures are listed as follows (Figure 2.8):

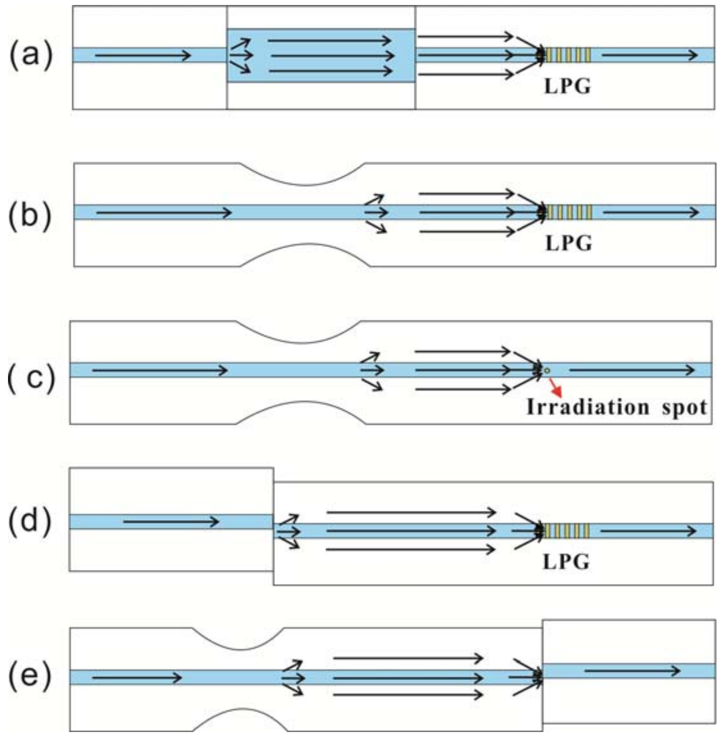

Figure 2.8 Various hybrid in-line fiber MZI. (a) Mode mismatch and LPG. (b) Taper and LPG. (c) Taper and Laser irradiation spot. (d) Core-offset and LPG. (e) Taper and core-offset.

A HMZI based on the mode mismatch and the LPG [76] is shown in Figure 2.8(a): In this work, a section of multi-mode fiber (MMF) was spliced with two single mode fibers and a LPG was made after the MMF. The mode mismatch due to the core size difference between MMF and SMF and LPG acted as two light steering elements to excite cladding modes and coupling them back to core mode to produce the interference signal. A curvature which can introduce phase shift to the sensor was performed upon the MMF. The phase of the interferometer was plotted as a function of the curvature magnitude, which showed a quite good linear relationship between them.

A HMZI based on the taper and the LPG [77] is shown in Figure 2.8(b): a fused taper and a LPG were made along a single-mode fiber with a separation of 80 mm. The taper waist diameter was controlled to be 80 μm and the period of LPG was 540 μm. This interferometer was successfully applied as an inclinometer. The axis of rotation went through the taper and the rotation angle was measured as a function of the interference pattern visibility.

A HMZI based on the laser irradiated spot and the taper [78] is shown in Figure 2.8(c): The spot was induced by a femtosecond laser which focuses the light beam in the center of fiber core. The separation between the spot and fused taper is set to be 10 mm. Temperature, strain and refractive index measurements were conducted using this sensor by monitoring selected peak wavelength shift.

Temperature and strain sensing is also realized by other types of HMZI, such as a combination of the core-offset and the LPG [79] as well as the taper and the core-offset [80] as shown in Figure 2.8(d)(e), and so on. These devices possess advantages of increased sensitivity and potential low cost as well as provide more selections for various sensing applications using fiber MZIs.

2.8 Summary of the state of art in-line fiber Mach-Zehnder interferometer

Table 2.1 lists the above mentioned several kinds of in-line fiber Mach-Zehnder interferometers and their state of art applications.

Sensor type	Fiber type	Measurands	Sensing performance
Tapered MZI	SMF	Strain[52]	2000nm/ε
		Simultaneous temperature and RI [53]	-23.188 nm/RIU, 0.071nm/^{o}C(169th order); -26.087nm/RIU, 0.077nm/^{o}C(144th order)
		Liquid level [54]	-0.017nm/mm (1520nm), -0.021nm/mm (1620nm)
		Lateral stress [55]	12.448×10^{-7} dBm/μm(A)
Mode-mismatch MZI	MMF and SMF	Temperature [57]	14.16pm/ ^{o}C
		Strain [57]	7pm/με
	High-order-mode fiber (HOMF) and SMF	Temperature [58]	—
		Strain [58]	—
Core-offset MZI	SMF	RI [8]	33.3nm/RIU
	PCF	Temperature [59]	—
		Strain [59]	—
	Hollow core fiber and SMF	Temperature [60]	11.085nm/ ^{o}C
		Strain [60]	1.5pm/ με
LPG MZI	SMF	Temperature [63]	0.31nm/ ^{o}C
		Thermo-optic	1.1×10^{-5}/^{o}C (GeO$_2$)

			coefficients [65]	0.75×10^{-5}/^{o}C (Boron)
		PCF [67]	—	—
Laser micromachined MZI		SMF (Femtoscond laser)	RI [37]	-3754.79 ± 44.24nm/RIU -12162.01 ± 173.92nm/RIU
		SMF (CO$_2$ laser)	RI [75]	—
			Temperature [75]	0.0817nm/ ^{o}C
Hybrid MZI	Mode-mismatch and LPG	MMF and SMF	Curvature [76]	612.44±3.12 Degree.m
	Taper and LPG	SMF	Rotation angle [77]	—
	Taper and laser spot	SMF	Temperature [78]	0.103nm/ ^{o}C (1593nm)
			Strain [78]	-1.35pm/ με (1593nm)
			RI [78]	-15.294nm/RIU(1593nm)
	Core-offset and LPG	SMF	Temperature [79]	0.0519nm/ ^{o}C
			Strain [79]	0.6pm/ με
	Taper and core-offset	SMF	Simultaneous temperature and strain [80]	60.4 and 63.9 pm/ ^{o}C -1.47 and -2.71 pm/ με

Table 2.1 State of art in-line fiber Mach-Zehnder interferometers

Based on previous work on in-line fiber Mach-Zehnder interferometers, our motivation for new-type sensors aims at improvement of the sensitivity to external perturbations, simplification of the fabrication process, enhancement of the mechanical strength and versatile selectivity for multi-parameter sensing. In the following two chapters, two novel sensors are proposed: one is tapered bend insensitive fiber Mach-Zehnder interferometer (BIF-MZI) and the other one is SMF-High-order-mode fiber-SMF Mach-Zehnder interferometer (HOMF-MZI), both of which belong to in-line MZI.

It is obvious the two novel sensors possess the advantages that the in-line fiber Mach-Zehnder interferometers have, such as compactness, simplicity, high integrity, light weight, low-cost and so on. The proposed BIF-MZI is the first in-line MZI that realizes the vibration sensing. The reason using bend insensitive fiber instead of standard SMF is due to the practical needs in vibration sensing and the unique double-cladding structure of BIF meets these requirements. In tapered SMF-MZI, the protective coating between the two tapers are removed to avoid the high attenuation loss of cladding modes. However, this coating-removed sensor has the difficulty to be applied in vibration measurement where a proper attachment between the sensor and the vibrating source is needed. Any touch to the coating-removed sensor would introduce large noise to the detected signal. While using bend insensitive fiber enables us to retain the protective coating and only limited inner-cladding modes are propagating along the sensor which guarantees a more uniform spectral response for dynamic vibration detection. Previous other types of fiber sensors used for vibration sensing include Fabry-perot interferometer, fiber Bragg grating and two fiber beams Mach-Zehnder interferometer. [81] presented a novel structure by splicing a short optical fiber stub containing a weakly tilted Bragg grating with another slightly offset fiber. The power reflected from this structure is independent of temperature. This device could obtain the frequency response up to 2 kHz. An in-line Fabry-perot interferometer was proposed by concatenating two fiber Bragg grating mirrors in [82]. The highest frequency measured was

1 kHz. In another work, two fiber beam Mach-Zehnder interferometer with one beam replaced by a long taper was presented as a vibration sensor [5]. Frequencies ranging from 30 Hz up to 40 kHz were measured with high SNRs. Compared to the above fiber vibrometers, the proposed sensor is sensitive to a much wider range of frequencies from 1 Hz up to 500 kHz with high SNRs above 20 dB. Nevertheless, this device still has some limitations, such as the frangibility of the taper structure and relative low contrast of transmission spectrum compared to other in-line MZIs.

Simultaneous temperature and strain measurements have been realized in many early works, such as using a single fiber Bragg grating [16], inscribing a long period grating in a polarization maintaining fiber [18], a Sagnac loop mirror consisting of two kinds of high-birefringence fibers [19] and a hybrid in-line fiber Mach-Zehnder interferometer [80]. Similar methods were employed in these works by monitoring the positions of resonant peaks in the transmission spectra under different temperatures or strains. However, exact determination of the resonant peak position is difficult in the transmission spectra whose fringes are usually results of superposition of multiple interferences. Besides, each interference has a unique dependence on temperature or strain, which would lead to nonlinear responses to the measurands. The usage of fiber Bragg grating, long period grating or Sagnac loop also increases the cost and complexity of sensor fabrication. The proposed HOMF-MZI is a good alternative and the discrimination of temperature and strain is by the first time achieved based on the dispersion effects of HOMF. Phase demodulation scheme is employed in this work instead of previous wavelength shift method to distinguish different interferences in the sensors. The strong chromatic dispersion effects of the supported modes in HOMF result in multiple peaks in spatial frequency domain, which provides a large amount of sensitivity choices for multi-parameter sensing. This sensor belongs to the mode-mismatch in-line MZI whose fabrication process is much easier and more repeatable than tapered structure. Furthermore, The mechanical strength of this device is much higher than other types of in-line MZI with no taper structure and all coating remained. However, this sensor cannot be utilized for refractive index sensing because of the remaining coating. Compared to SMF based in-line MZI, the HOMF-MZI has a higher cost.

Chapter 3

Vibration sensing using a tapered bend-insensitive fiber based Mach-Zehnder interferometer

This chapter presents a novel fiber-optic sensor consisting of a tapered bend-insensitive fiber based Mach-Zehnder interferometer (BIF-MZI) to realize damped and continuous vibration measurements. A high sensitivity and fast response intensity based demodulation scheme is adopted by monitoring power fluctuation of the BIF-MZI at the operation wavelength. The double cladding structure and the central coating region of the in-fiber interferometer ensure an enhanced mechanical strength, reduced external disturbance, and a more uniform spectrum. A damped vibration frequency range of 29-60 Hz as well as continuous vibration disturbances ranging from 1 Hz up to 500 kHz are successfully demonstrated. Section 3.1 gives the background of vibration sensing based on fiber sensors and tapered BIF-MZI. Section 3.2 explains in detail the operation principle based on intensity demodulation scheme. Section 3.3 describes the fabrication process of the proposed device and the configuration of vibration experimental setup. Section 3.4 shows experimental results and discussions of damped and continuous vibration respectively in two subsections. The final conclusion comes in section 3.5.

3.1 Introduction

Detection and monitoring of vibration, acceleration, and mechanical shock are crucial for nondestructive inspection of civil infrastructures such as buildings, bridges, highway pavements, and dams, structural health monitoring of automobiles, ships, aircraft, and spacecraft, as well as environmental surveillance of seismic activity and volcanic eruptions. A piezoelectric accelerometer is the most conventional vibration sensor for structural monitoring which utilizes the piezoelectric effect to measure dynamic changes in mechanical variables. However a lack of an effective electrical isolation scheme makes it unsuitable in a total electromagnetic sensitive environment. A fiber optic sensor will be a good alternative over its electric counterpart with several unique advantages, such as immunity to electromagnetic interference, compact size, light weight, and distributed measurement over a long distance [83]. A variety of fiber optic sensing techniques have been extensively studied and among them, in-fiber Mach-Zehnder interferometer (MZI) sensors have recently been applied to measure temperature, strain, pressure, and refractive index with salient merits of high sensitivity, a high degree of integration, simplicity, and compact in-line measurement [52, 59, 76, 84-92]. For these static measurements, the fiber sensors rely on the demodulation of external disturbance induced interference peak wavelength shift, which needs a relatively long time to obtain a steady spectrum. Thus the spectral shift detection algorithm with a slow response time is not suitable for sensing a rapidly and dynamically changing environment, such as shock impulses and mechanical vibrations. In addition, previously reported in-fiber MZIs are required to remove protective jackets between two light steering elements in order to prevent the excited cladding modes from suffering high attenuation loss. Consequently the fiber mechanical strength is reduced and the uncoated fiber cladding layer is directly exposed to the surrounding environment which leads the fiber interferometer to be vulnerable to undesirable disturbance.

In recent years, various types of bend-insensitive fibers (BIF) have been developed to allow for better light confinement at a smaller bending radius with ultralow bending loss in Fiber-to-the-Home applications [93-98]. High-order cladding modes can be excited by an optical connection with an imperfect mode match between two fibers and to be guided by a structure of a depressed-index area [99, 100]. If the high-order modes are not fully attenuated as they propagate along the fiber, they may couple back to the core at a following optical connection to induce a multipath-interference phenomenon. Suppression of excited high-ordercladding modes and minimization of modal interference with the fundamental mode could be implemented using mode strippers realized by filling a section of air holes with epoxy [101]. In this paper, a novel tapered bend-insensitive fiber based in-line Mach-Zehnder interferometer (BIF-MZI) is fabricated by a fusion splicing technique for damped and continuous vibration sensing applications. An intensity-based demodulation scheme is developed to monitor the dynamic vibration induced power fluctuation at a specific wavelength selected from the transmission spectrum of the BIF-MZI.

3.2 Operation principle

The bend-insensitive single-mode fiber (ClearCurve, Corning) used in this study comprises an innermost layer of a germanium-doped silica core surrounded by a narrow layer of randomly distributed air holes in the pure silica cladding [96]. A schematic of the bend-insensitive fiber cross-section in Figure 3.1 shows that the depressed index ring of nanoscale gas filled voids divides the fiber cladding region into two areas of an inner cladding region and an outer cladding region. A schematic illustration of the BIF-MZI is shown in Fig. 3-1. The BIF-MZI consists of two abrupt tapers which function as light steering elements to pilot split-merge propagation of the fundamental core mode and high-order cladding modes along the middle fiber section between the two fiber tapers. The double cladding structure of the bend-insensitive fiber enables a selective excitation of multiple cladding modes by the first taper. According to mode field patterns, the cladding modes of the bend-insensitive fiber can be categorized into two groups: inner-cladding modes that travel within the inner cladding region due to the total internal reflection and outer-cladding modes that tunnel into the outer cladding region through the depressed index ring. When the polymer coating is removed from the middle fiber section, both the inner-cladding modes and the outer-cladding modes excited by the first taper will be coupled back to the core mode by the second taper to form a fiber Mach-Zehnder interferometer. The phase difference ΔΦ between the fundamental core mode of LP_{01} and multiple high-order cladding modes of LP_{ij} can be expressed as

$$\Delta\Phi_{ij} = \Phi_{core,01} - \Phi_{clad,ij} = \frac{2\pi l}{\lambda}(n_{eff}^{core,01} - n_{eff}^{clad,ij}) = \frac{2\pi l}{\lambda}\Delta n_{eff}^{ij}, \tag{3.1}$$

where $\Delta n^{ij}{}_{eff}$ is the effective refractive index difference between the fundamental core mode and an individual high-order cladding mode, l is the interference length, and λ is the operation wavelength. When the phase difference satisfies $\Delta\Phi_{ij} = 2m\pi$, the m^{th} order transmission peak wavelength is located at

$$\lambda_m = \frac{\Delta n_{eff}^{ij} l}{m}, \tag{3.2}$$

where *m* is an integer. The intensity in the interference pattern can then be written as

$$I(\lambda) = I_{core,01} + I_{clad,ij} + 2\sqrt{I_{core,01} I_{clad,ij}} \cos(\Delta\Phi_{ij}) \tag{3.3}$$

where $I_{core,01}$ and $I_{clad,ij}$ are the intensities of the fundamental core mode and an individual high-order cladding mode, respectively. Provided that the polymer coating between the two abrupt tapers is retained in the process of fabricating a BIF-MZI, optical energy in the outer-cladding modes would be sharply attenuated due to high refraction loss at the unsmoothed cladding-coating interface and a significant absorption band in the telecommunication window of the high index polymer coating, while energy in the inner-cladding modes could still travel down the inner cladding region with little attenuation and reach the second taper. Thus a novel in-fiber Mach-Zehnder interferometer will be developed based on a tapered bend-insensitive fiber while still preserving its original protective jacket.

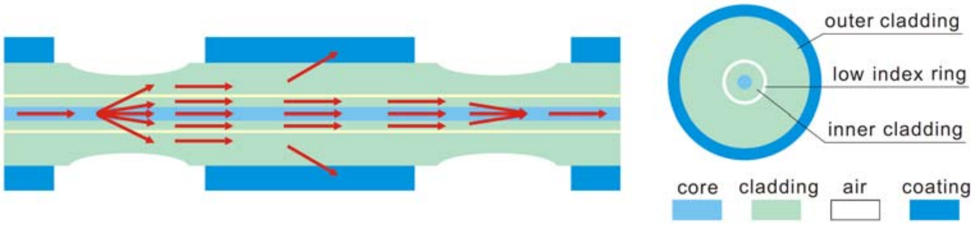

Figure 3.1 Left: A schematic illustration of the bend-insensitive fiber based Mach-Zehnder interferometer. Right: A schematic cross-section of the bend-insensitive fiber.

As a mechanical strain ε is applied on the BIF-MZI, the changing phase difference between the core mode and each cladding mode will lead to a shift in the corresponding spectrum where an interference peak wavelength λ_m shifts to a new wavelength of λ_m' by

$$\begin{aligned}\Delta\lambda_m &= \lambda_m' - \lambda_m = \frac{\left(\Delta n_{eff}\delta l + \delta n_{eff} l + \delta n_{eff}\delta l\right)}{m} \approx \lambda_m \frac{\left(\Delta n_{eff}\delta l + \delta n_{eff} l\right)}{\Delta n_{eff} l} \\ &= \lambda_m(\delta l / l + \delta n_{eff} / \Delta n_{eff}) = \lambda_m(\delta l / l + p_{eff}\delta l / l) = \lambda_m(1 + p_{eff})\varepsilon,\end{aligned} \tag{3.4}$$

where δl is the variation of the fiber length due to the axial strain, δn_{eff} is the photo-elastic effect induced change in the effective refractive index difference, and p_{eff} is the effective strain-optic coefficient. When a tapered bend-insensitive fiber is mounted on a cantilever, the fiber length will increase or decrease when the cantilever undergoes a convex or concave deflection as shown in Figure 3.2(a). The change in the interference length δl of the BIF-MZI can be expressed as $\delta l \approx 2dD/l$, where D is the cantilever deflection and d is the separation of the neutral axis between the optical fiber and the steel cantilever. Thus damped vibrations of the cantilever will cause a dynamic strain variation on the BIF and a fluctuation in power spectrum of the BIF-MZI. In case a piezoelectric cylinder is used to provide a continuous dynamic strain on the tapered bend-insensitive fiber by wrapping the fiber on it as shown in Figure 3.2(b), the transmission spectrum of the BIF-MZI will periodically red-shift or blue-shift when the fiber interferometer length experiences an elongation or compression due to the piezoelectric effect of the lead zirconate titanate (PZT) ceramic material. Figure 3.2(c) shows a schematic illustration of fiber interferometer vibration sensing based on an intensity modulation scheme. According to a typical sinusoidal variation of the output intensity of a two-mode interferometer as a function of wavelength, a linear intensity response can be acquired for low-amplitude vibrations observed at a quadrature bias wavelength.

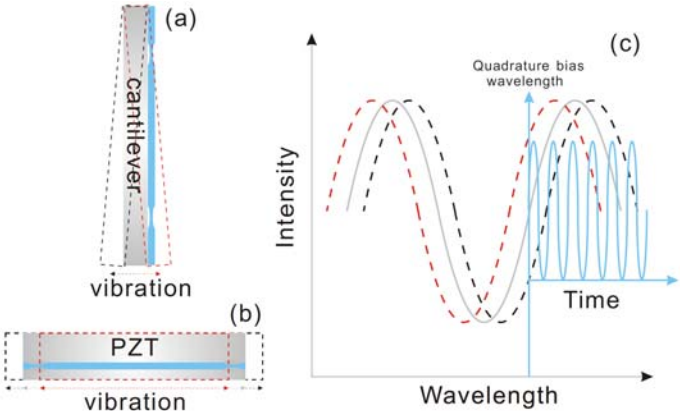

Figure 3.2 A schematic illustration of fiber interferometer vibration sensing based on an intensity modulation scheme.

3.3 Experimental configuration

In the vibration sensing systems, the in-fiber Mach-Zehnder interferometer was fabricated on the bend-insensitive fiber that was connected to two standard single-mode fibers (SMF28, Corning) on both sides to form a SMF-BIF-SMF structure. If a mechanical splicing method is adopted such as using optical fiber connectors, a splice loss modulation will result in weak modal interference due to a refractive index profile difference induced mode-field mismatch between the SMF and the BIF. Therefore the SMF-BIF-SMF structure was implemented based on a fusion splicing technique using a fusion splicer (S182PM, Fitel). A customized clad alignment fusion splicing program with appropriate fusion current and fusion time was employed to line up the fibers, minimize the splice loss and avoid the modal interference. The electrical arc discharge zone was adjusted to introduce an offset of 10 μm deviated from the junction point to the SMF side, which could accommodate the presence of the nanostructural features and guarantee the intactness of the air-hole structure of the BIF during the fusion splicing process. Figure 3.3(a) shows an optical microscope image of the fusion joint area between the SMF and the BIF where they are in good alignment. Intermodal interference was not detected in the output spectrum of the SMF-BIF-SMF structure by launching light from a combined C + L band erbium-doped fiber amplifier (EDFA) to an optical spectrum analyzer (86142A, Agilent). Another fusion splicer (FA995, Ericsson) with a built-in taper manufacturing program was utilized to fabricate fiber tapers on the bend-insensitive fiber. Selecting a taper specification of a large waist diameter should ensure that fiber mode coupling efficiency is small and thus the attenuation of the interferometer is minimized and fewer high-order modes are excited [102]. An optical microscope image of an abrupt taper with a taper length of 900 μm and a waist diameter of 80 μm is shown in Figure

3.3(b). Two individual in-fiber MZIs, BIF-MZI-a and BIF-MZI-b, were constructed along the bend-insensitive fibers by creating double abrupt tapers of the above specifications separated by distances of 5 cm and 15 cm, respectively.

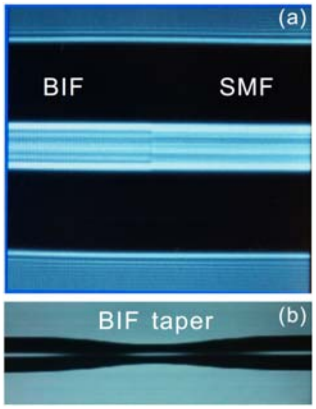

Figure 3.3 (a) An optical microscope image of the fusion joint area between the BIF (left) and the SMF (right). (b) An optical microscope image of one abrupt taper fabricated on the BIF.

Figure 3.4(a) shows the attenuation spectrum of the BIF-MZI-a which was obtained from the difference between the emission spectrum of the EDFA and the transmission spectrum of the BIF-MZI. Although the central coating region was preserved, the tapered bend-insensitive fiber still performed well as an in-fiber interferometer which is evident from the prominent interference fringes due to a superposition of several inner-cladding modes interferences. A fast Fourier transform (FFT) of the wavelength spectrum in Fig. 3.4(a) provides a spatial frequency spectrum as shown in Fig. 3.4(b). The spatial frequency ξ can be expressed as $\xi \approx \Delta n_{eff}L/ \lambda_0^2$, where λ_0 is the center peak wavelength around which a first-order Taylor series is expanded [59]. In Fig. 3.4(b), a power spectrum in the spatial frequency domain exhibits two dominant intensity peaks corresponding to two inner-cladding modes with their corresponding simulated optical field patterns shown in the inset of Fig. 3.4(b). It is noticed that the light energy of the inner-cladding modes are completely confined in the inner cladding region. Figure 3.4(d) shows a spatial frequency spectrum of the BIF-MZI-b with two dominant intensity peaks obtained by fast Fourier transform of the corresponding attenuation spectrum in Fig. 3.4(c). The simulated optical field patterns of the inner-cladding modes are shown in the inset of Fig. 3.4(d). Since the BIF-MZI allows only very few inner-cladding modes to pass through the central fiber coating region, the superimposed interference spectrum of this few-mode interferometer still monotonically shifts with a changing strain and thus the power fluctuation at the operation wavelength exhibits an approximate linear response relation to dynamic vibrations. Compared to the conventional in-fiber MZIs based on a standard single-mode fiber with a single cladding layer, the BIF-MZI has very few order numbers of interference due to its double cladding structure and central coating region, and accordingly a more uniform spectrum which is suitable for dynamic vibration sensing applications.

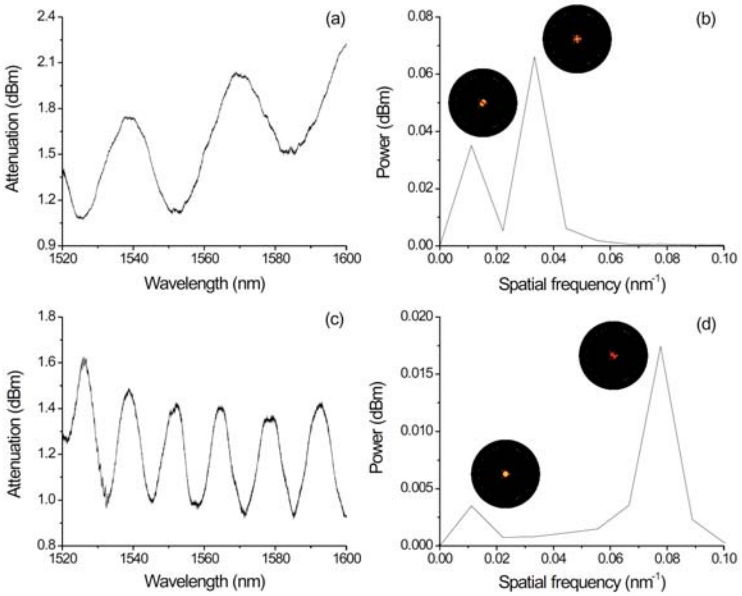

Figure 3.4 (a, b) and (c, d) show attenuation spectra and corresponding spatial frequency spectra of the BIF-MZI-a and BIF-MZI-b, respectively. Insets of (b, d) show the simulated optical field patterns of the inner-cladding modes of BIF-MZI-a and BIF-MZI-b.

Figure 3.5 shows a schematic experimental setup of vibration measurement using the BIF-MZI. Light from a 1550 nm planar waveguide based external cavity laser with the 3 kHz spectral linewidth (PLANEX, Rio) was launched into the BIF-MZI and then guided through an attenuator and an AC photodetector (PDB450C-AC, ThorLabs) to a high-speed oscilloscope (WaveRunner 64Xi-A, LeCroy). Experiments were carried out in a temperature controlled room with the temperature maintained at 25.0 ± 0.5 ^{o}C. The temperature change can be neglected since it is a rather slow process relative to the dynamic vibration measurement with a fast response. At a specific operation wavelength, 1550 nm for example, the changing power due to vibrations becomes a strong function of time. By monitoring the power variation in a time domain, the vibration frequency could be detected in real time.

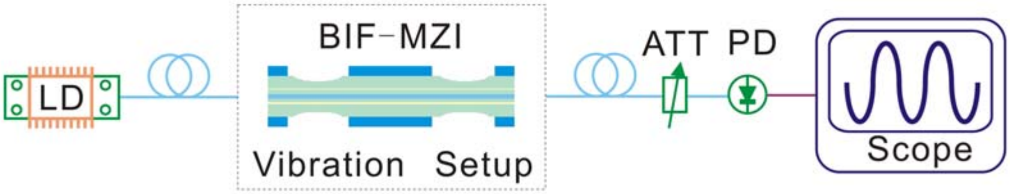

Figure 3.5 A schematic experimental setup of vibration measurement. LD, laser diode; ATT, attenuator; PD, Photodetector.

3.4 Experimental results and discussion

3.4.1 Detection of damped vibration

Figure 3.6 shows a schematic measurement setup to detect damped vibration frequency using the 5 cm BIF-MZI-a. A stainless steel cantilever of rectangular cross-section (width w = 0.5 cm, thickness h = 0.1 cm) and a total length of 40 cm was used to generate a damped vibration. The tapered bend-insensitive fiber was slightly pre-stretched and attached to the free end of the steel cantilever using epoxy glue. The set point of the pre-strained value was about 103 με, which was selected to avoid fiber breakage or movement during a convex or concave deflection process. Another end of the cantilever was fastened on a fixed base by a metal clamp and the cantilever length could be controlled by adjusting the position of the metal clamp on the cantilever. When the free end of the cantilever was deflected by a specific displacement from its initial stabilized position and instantly released, the cantilever would experience a damped vibration about its equilibrium position soon afterwards. A standard ruler was used to measure the initial deflection of the cantilever.

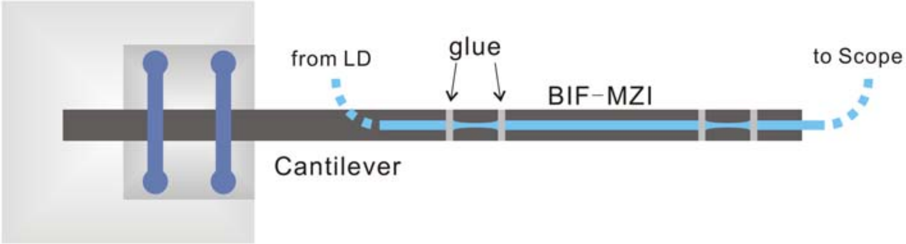

Figure 3.6 Schematic top view of the experimental setup of damped vibration detection.

Figures 3.7(a) and 3.7(c) show the time-domain spectra of the BIF-MZI-a with a 10 cm cantilever length under damped vibrations that the free end of the cantilever were initially flipped down to a distance of 5 mm and 3 mm, respectively. Figure 3.7(a) shows that the initial output voltage recorded by the oscilloscope is 0.12 V for the damped vibration of the 5 mm deflection. As the vibration continued, the damping effect caused a continuous attenuation of the output voltage with a specific damping time defined as a timescale for an output voltage dropping to 90% of its initial value. The vibration finally vanished and a noise floor was obtained with a stable output voltage of 0.01 V. The damping time was measured to be 5.0 seconds by performing an envelope analysis on the time-domain signal shown by the red curves in Fig. 3.7(a). For the damped vibration of the 3 mm deflection, a relatively small initial peak voltage of 0.06 V and a damping time of 4.0 seconds were obtained in Fig. 3.7(c). In addition, two insets of Figs. 3.7(a) and 3.7(c) extracted from enlarged regions of the vibration time trace signal exhibit regular sinusoidal waveforms which indicate a stable periodicity of the power oscillations. Figures 3.7(b) and 3.7(d) show the same fundamental frequency of 62.0 Hz by fast Fourier transform of the time-domain spectra in Figs. 3.7(a) and 3.7(c). When the initial deflection of the cantilever was varied from 1 mm to 7 mm, the fundamental frequencies were in the range from 61.8 ± 0.5 Hz to 62.4 ± 0.5 Hz as shown in Fig. 3.7(e). It is indicated that the fundamental frequencies of the damped vibrations is independent of the initial deflection of the cantilever.

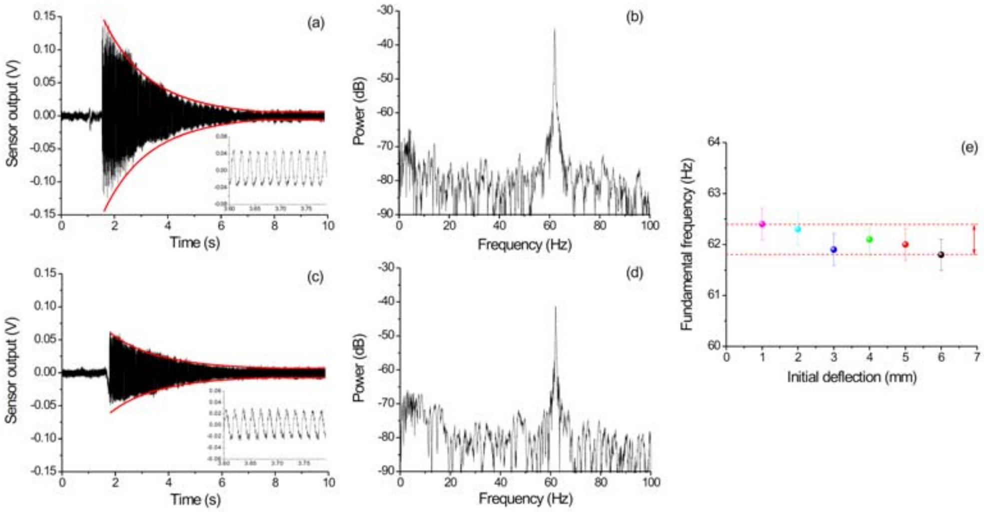

Figure 3.7 Time-domain spectra and frequency-domain spectra of the BIF-MZI-a with a cantilever length of 10 cm under damped vibrations of (a, b) 5 mm and (c, d) 3 mm deflections, respectively. (e) Fundamental frequencies as a function of initial deflections of the cantilever.

Various fundamental frequencies of the damped vibrations can be obtained by changing the cantilever length. The fundamental frequency should be proportional to the reciprocal of the square of the cantilever length, which follows

$$f = \frac{c}{2\pi}\sqrt{\frac{EI}{\rho A L^4}}, \tag{3.5}$$

where c is the coefficient of the first vibration mode, E is the Young's modulus of the stainless steel, I is the moment of inertia, ρ is the density of the material, A is the cross section area, and L is the cantilever length. The damped vibrations of different cantilever lengths under the same initial deflection were detected using the BIF-MZI-a to demonstrate this relationship. Figure 3.8(a) shows the time-domain spectrum of the BIF-MZI-a with a cantilever length of 15 cm under a damped vibration of a 3 mm deflection and Fig. 3.8(b) shows the corresponding frequency-domain spectrum where the fundamental frequency was located at 29.2 Hz. The normalized power spectra of the BIF-MZI-a with six different cantilever lengths ranging from 10 to 15 cm are shown in Fig. 3.8(c). Figure 3.8(d) shows a linear relationship between f and $1/L^2$, where the fundamental frequencies corresponding to these cantilever lengths are 62.0 Hz, 52.8 Hz, 44.1 Hz, 38.5 Hz, 33.0 Hz, and 29.2 Hz, respectively.

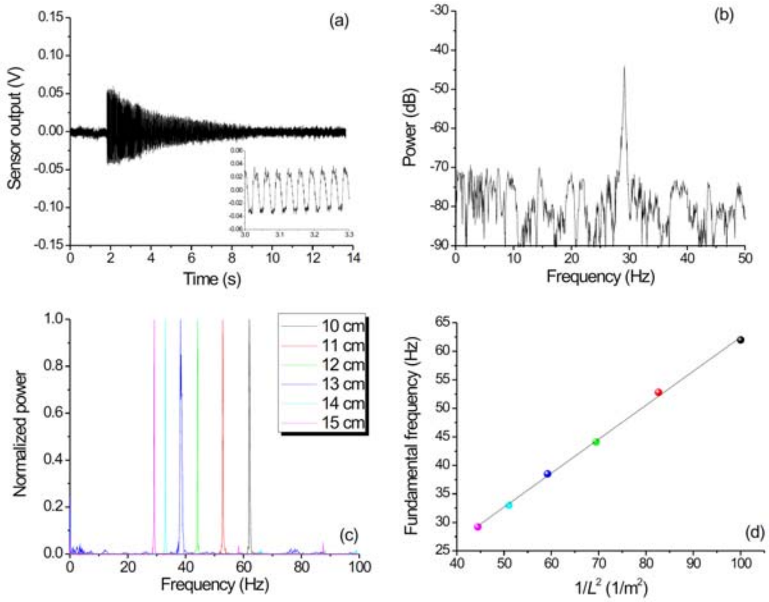

Figure 3.8 (a) Time-domain spectrum of the BIF-MZI-a with a cantilever length of 15 cm under a damped vibration of 3 mm deflection and (b) the corresponding frequency-domain spectrum. (c) Normalized power spectra of the BIF-MZI-a with different cantilever lengths. (d) Fundamental frequencies as a function of cantilever lengths.

3.4.2 Detection of continuous vibration

Figure 3.9 shows a schematic setup to measure a continuous vibration frequency using the 15 cm BIF-MZI-b. A piezoelectric cylinder (Americanpiezo) with an external diameter of

38 mm was utilized as a continuous vibration source driven by a function generator. The piezoelectric cylinder has a frequency response range up to a maximum of 500 kHz. The central coating region of the tapered bend-insensitive fiber was wound around the piezoelectric cylinder and tightly bonded on the exterior surface using epoxy glue. The double abrupt taper regions were attached on two fixed bases and slightly stretched to keep the fiber straight. A periodic sinusoidal driven signal with a peak-to-peak voltage of 10 volts caused a continuous vibration of the piezoelectric cylinder that was transmitted to the fiber and generated about 1 micro-strain equivalent dynamic stretch.

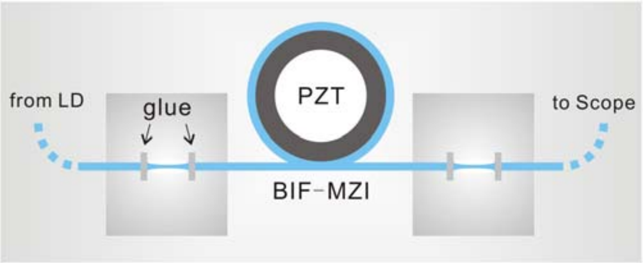

Figure 3.9 Schematic top view of the experimental setup of continuous vibration detection.

Firstly the BIF-MZI-b underwent low frequency vibrations of the piezoelectric cylinder. Figures 3.10(a)—3.10(d) show the frequency-domain spectra of the BIF-MZI-b when the piezoelectric cylinder was driven by sinusoidal signals of 1.0 Hz, 3.0 Hz, 5.0 Hz, and 10.0 Hz, respectively, and the corresponding time-domain spectra are shown in the insets. In the frequency-domain spectra, dominant peaks are located at 1.0 Hz, 3.0 Hz, 5.0 Hz, and 9.5 Hz, respectively, which are close to their corresponding driven frequencies. In Fig. 3.10(d), three other peaks at frequencies of 19.0 Hz, 29.0 Hz, and 38.5 Hz are obviously distinguished beyond the fundamental frequency of 9.5 Hz which agrees well with the high-order harmonics resonance phenomenon.

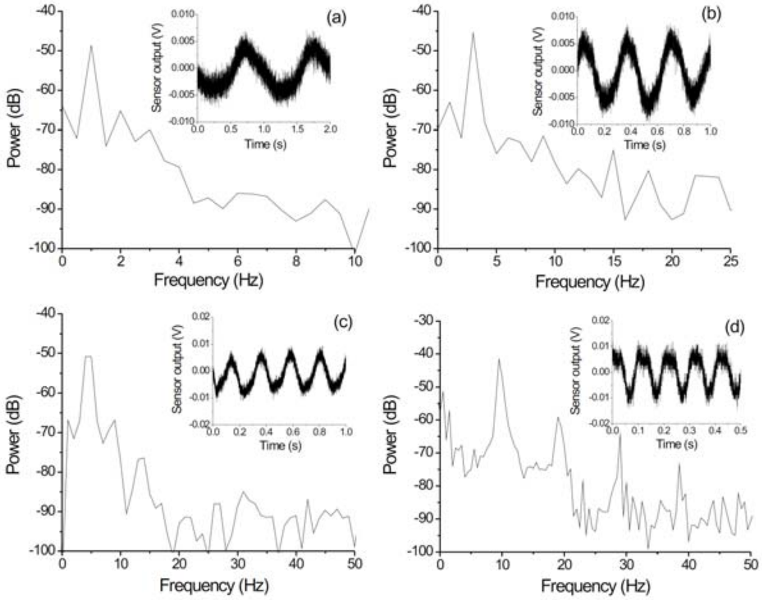

Figure 3.10 (a, b, c, and d) show the frequency-domain spectra of the BIF-MZI-b when the piezoelectric cylinder was driven by sinusoidal signals of 1 Hz, 3 Hz, 5 Hz, and 10 Hz, respectively. The insets show the corresponding time-domain spectra.

The vibration frequency of the piezoelectric cylinder was then tuned from 100 Hz to 15 kHz. Figures 3.11(b) and 3.11(e) show two enlarged regions of the vibration time trace signal extracted from Figs. 3.11(a) and 3.11(d) which present good sinusoidal waveforms with a constant power oscillation periodicity. Figure 3.11(c) plots the frequency-domain spectrum from Fourier transform of the corresponding 0.8 seconds time-domain data with a peak at 98.9 Hz when the piezoelectric cylinder was driven by a 100 Hz sinusoidal signal. Figure 3.11(f) shows a FFT spectrum with a peak at 15.0 kHz as the piezoelectric cylinder was driven by 15 kHz sinusoidal wave. Figures 3.11(c) and 3.11(f) show high signal-to-noise-ratios (SNR) of 45 dB and 50 dB, respectively. When the driven frequencies of the piezoelectric cylinder were set to 500 Hz, 1 kHz, 5 kHz, and 10 kHz, the corresponding FFT spectra had obvious peaks with SNRs of 50 dB at 497.9 Hz, 998.9 Hz, 4.99 kHz, and 9.98 kHz, respectively.

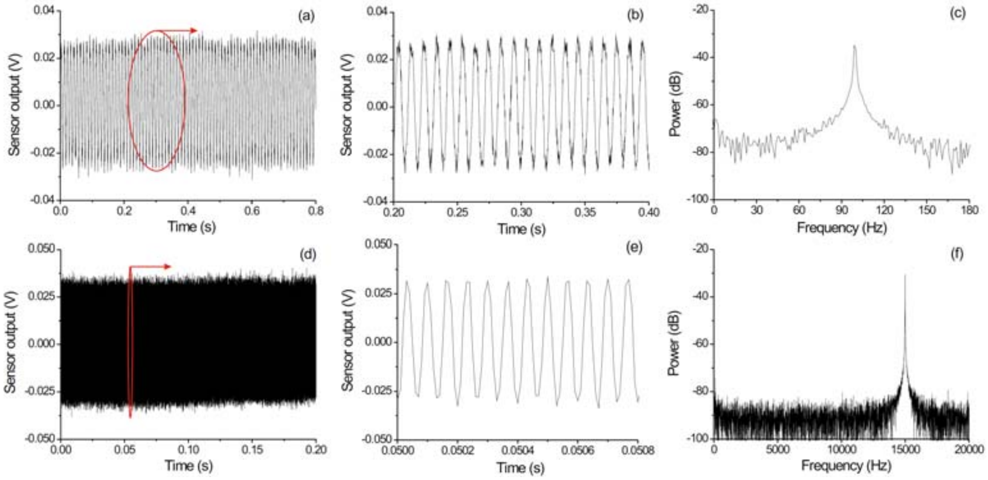

Figure 3.11 (a, b) and (d, e) show the time-domain spectra as well as (c) and (f) the corresponding frequency-domain spectra of the BIF-MZI-b when the piezoelectric cylinder was driven by sinusoidal signals of 100 Hz and 15 kHz, respectively.

High frequency continuous vibrations of the BIF-MZI-b were investigated by tuning the vibration frequency of the piezoelectric cylinder up to 500 kHz. Figure 3.12 shows obvious peaks in the FFT spectra with high SNRs from 40 dB to 50 dB at 99.96 kHz, 199.91 kHz, 299.89 kHz, 399.88 kHz, and 499.78 kHz, respectively, as the driven frequencies of the piezoelectric cylinder were increased from 100 kHz to 500 kHz in 100 kHz steps.

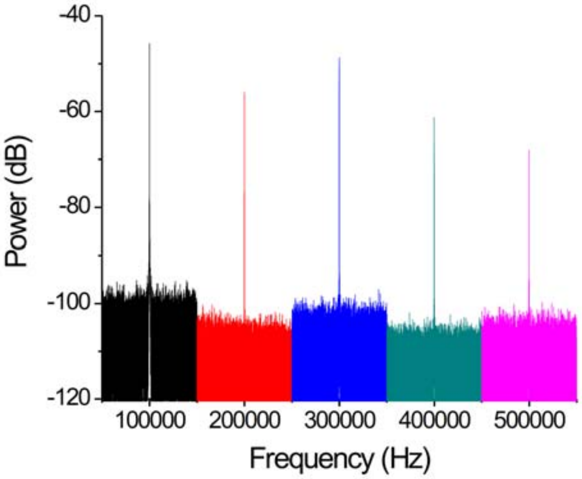

Figure 3.12 The frequency-domain spectra of the BIF-MZI-b when the piezoelectric cylinder was driven by high frequency sinusoidal signals from 100 kHz to 500 kHz.

3.5 Conclusion

In conclusion, a tapered bend-insensitive fiber interferometer sensor has been proposed and experimentally demonstrated. A high sensitive and fast response intensity based demodulation scheme has been adopted by monitoring power fluctuation of the BIF-MZI at the operation wavelength to detect damped and continuous vibrations. The possibility of manufacturing an in-fiber Mach-Zehnder interferometer without removing its central protective jacket provides many great advantages in vibration sensing applications, such as maintaining high mechanical strength, isolating the optical fiber from external physical damage, and allowing easy fiber attachment to a substrate. Furthermore, attenuated outer-cladding modes due to optical coating absorption leaves a few inner-cladding modes propagating along the bend-insensitive fiber and a more uniform spectral response is available for dynamic vibration sensing. The in-fiber interferometer sensor has an extremely wide frequency response from 1 Hz up to 500 kHz. The experimental results imply that the proposed BIF-MZI could be effectively employed in applications on intrusion detection and structure health monitoring.

Chapter 4

Dispersion effects of high-order-mode fibers on temperature and axial strain discrimination

This chapter proposes a new technique based on the chromatic dispersion effect of high-order-mode fibers (HOMFs) to simultaneously measure the temperature and strain. The wavelength dependent chromatic dispersion of the supported core modes in HOMF is characterized and the critical wavelength is theoretically found and experimentally verified. By performing fast Fourier transform upon transmission spectrum and using a phase demodulation scheme, different sensitivities of different wavelength dependent dispersion peaks in spatial frequency domain responding to dual or more environmental disturbances have been demonstrated. Section 4.1 gives the background of the high-order-mode fiber and the discrimination of stain and temperature. Section 4.2 presents the mode analysis and the dispersion effect in HOMF using simulation method. Section 4.3 describes the proposed method for mode discrimination in experimental transmission spectra. Section 4.4 explains the sensing principle and discussed the experimental results. Section 4.5 concludes the whole work.

4.1 Introduction

High-order-mode fibers (HOMFs) have been broadly investigated for practical applications in dispersion compensation, enhancement of fiber transmission and data capacity, mode filters and selectors, and fiber sensors [103-107]. One of the most significant properties of HOMF is the relative stable existence of several core modes which exhibit considerable dispersion effect. Therefore the mode analysis and chromatic dispersion characterization are vital to enhance the performance of fiber sensors based on HOMF. The discrimination between temperature and strain is vital in many applications and has attracted great interest recently [18, 19, 108-110]. In this chapter, the realization of a discrimination measurement between temperature and strain is presented based on dispersion effect under a novel phase demodulation scheme. The dispersion effect gives the versatile sensitivities to environmental changes and possesses the potential for the device to be utilized as a multi-parameter sensor.

4.2 Simulation results of mode analysis and dispersion effects in HOMF

Figure 4.1 presents a refractive index profile of a custom designed HOMF calibrated by an optical fiber analyzer (NR-9200, EXFO) based on the standard refracted near-field technique. The refractive index of the pure silica cladding region is measured to be 1.4560 ± 0.0001 at 670 nm. Scanning electron microscopy (SEM) images of the transversal cross-section of the HOMF are shown in the inset of Fig. 4.1. The HOMF was etched with 5% hydrofluoric acid solution for 5 minutes to enhance contrast and visibility of the SEM images because of different etch rates of fiber regions with varied dopant concentrations. It is obvious that the complex fiber core structure consists of four distinct layers where the central layer is further divided into three subsections. The unique refractive index profile of the HOMF can support multiple core modes with tailored dispersion properties. Two standard single-mode fibers (SMF-28, Corning) are fusion spliced on both sides of the HOMF to form a SMF-HOMF-SMF structure. When a fundamental mode light beam is incident from the input SMF to the sandwiched HOMF, a few guided core modes will be excited due to mode field mismatch. Provided that the SMF and the HOMF are perfectly aligned, only circularly symmetric LP$_{0m}$ modes are preferably supported in the HOMF because of the circular symmetry of the input field of the LP$_{SMF}$ mode in the SMF. Interference between these modes dictates the output spectral response of the proposed HOMF modal interferometer, which is vulnerable to influences of the environmental parameters such as temperature and axial strain.

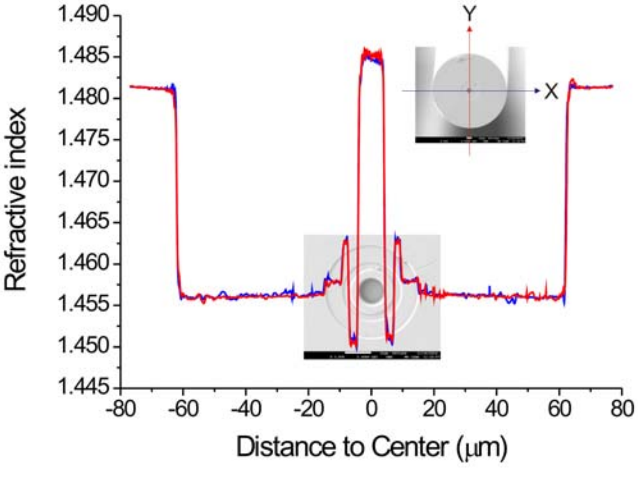

Figure 4.1 A calibrated refractive index profile of the HOMF at 670 nm; blue and red curves correspond to scans along two orthogonal axes of its transversal cross-section, X-axis and Y-axis, respectively, inset: SEM images of the etched HOMF over the whole cross-sectional area and the central core region.

Modal analysis in the HOMF is achieved by employing the COMSOL Multiphysics finite element analysis software to numerically simulate the effective indices of the multiple core modes as a function of wavelength, from which intermodal dispersion and chromatic dispersion properties can be derived. The simulated mode field patterns of the input fundamental core mode of the SMF as well as the excited core modes of the HOMF at 1550 nm are shown in the insets of Figs. 4.2(c) and 4.2(d). The vector overlap integrals of the two mode fields are performed using the equation [111],

$$\eta = \frac{\left| \iint E_{\mathrm{SMF}}(x,y) E_{\mathrm{0m}}^{*}(x,y)\, dxdy \right|^{2}}{\iint E_{\mathrm{SMF}} E_{\mathrm{SMF}}^{*}\, dxdy \iint E_{\mathrm{0m}} E_{\mathrm{0m}}^{*}\, dxdy}, \tag{4.1}$$

where ESMF and E0m are the complex electric fields of the fundamental mode in the SMF and individual excited core modes in the HOMF, respectively. Coupling efficiencies between the LP_{SMF} mode and the LP_{01}, LP_{02}, and LP_{03} modes are calculated to be 74.2%, 18.4%, and 6.4%, respectively. The dominant LP_{01} mode can couple with the LP_{02} and LP_{03} modes with a strong field overlap. Since the first three excited core modes account for 99.0% of the incident mode energy, the coupling of light between the LP_{01} mode and higher-order core modes ($m > 2$) as well as the LP_{01}-LP_{02} mode coupling is negligible.

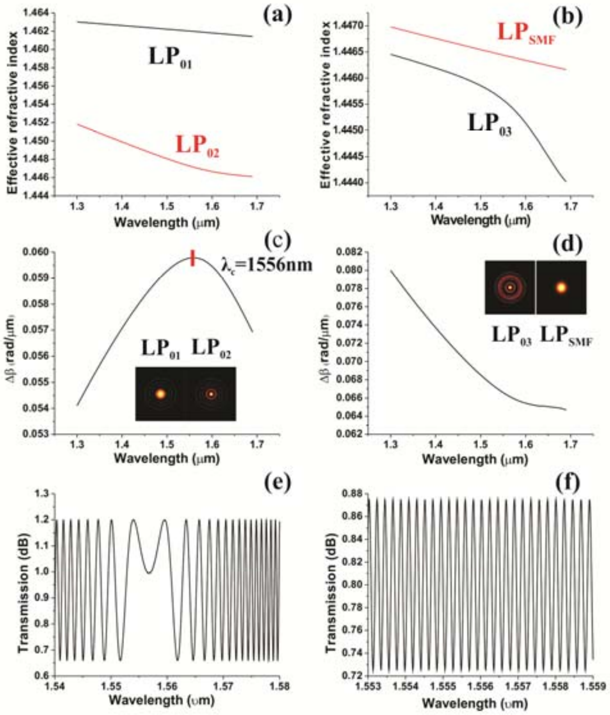

Figure 4.2 Wavelength dependent effective refractive indices of (a) the LP_{01} and LP_{02} modes, (b) the LP_{03} and LP_{SMF} modes; Difference in the propagation constant as a function of wavelength between the LP_{01} mode and (c) the LP_{02} mode, (d) the LP_{03} mode, insets of (c) and (d): mode field patterns of the LP_{01} and LP_{02} modes, and the LP_{03} and LP_{SMF} modes; (e) and (f) show transmission spectra of a 1-meter HOMF modal interferometer with the LP_{01}-LP_{02} and LP_{01}-LP_{03} mode coupling, respectively.

The relationship between the effective indices of the first three core modes and wavelength are shown in Figs. 4.2(a) and 4.2(b). The negative slopes of these three curves follow the same trend of change in the wavelength dependent modal effective index of the fundamental mode in the standard single-mode fiber as shown in Fig. 4.2(b). The difference in the propagation constant between two coupling modes is given by

$$\Delta\beta_{2(3)} = \beta_1 - \beta_{2(3)} = k[n_1(\lambda) - n_{2(3)}(\lambda)] = k\Delta n_{2(3)}(\lambda), \qquad (4.2)$$

where $k = 2\pi/\lambda$ is the wavenumber, $n_1(\lambda)$, $n_{2(3)}(\lambda)$, and $\Delta n_{2(3)}(\lambda)$ are the wavelength dependent modal effective indices of the first-order core mode, the second- or third-order core modes, and their effective index difference, respectively. The intensity in the interference pattern can be written as

$$I = I_1 + I_{2(3)} + 2\sqrt{I_1 I_{2(3)}} \cos\left(\Delta\Phi_{2(3)}(\lambda)\right), \qquad (4.3)$$

where I_1 and $I_{2(3)}$ are the intensities of the first-order and the second- or third-order core modes, respectively, and $\Delta\Phi_{2(3)}(\lambda)$ is the phase difference between the LP_{01} and the LP_{02} or LP_{02} modes with an expression of $\Delta\Phi_{2(3)}(\lambda) = \Delta\beta_{2(3)}L$, where L is the length of the HOMF. Figure 4.2(c) shows the propagation constant difference between the LP_{01} and the LP_{02} modes as a function of wavelength, where a vertex oriented upwards existing in the parabolic curve at around 1556 nm that corresponds to a critical wavelength in the transmission spectrum induced by the LP_{01}-LP_{02} mode interference. Then a normalized transmission spectrum of a 1-meter HOMF modal interferometer can be simulated by applying a polynomial curve fitting to the plot of the wavelength dependent propagation constant difference shown in Fig. 4.2(e). The propagation constant difference between the LP_{01} and the LP_{03} modes as a function of wavelength is shown in Fig. 4.2(d), where no turning point is found and only a monotonic decline curve is observed within the same wavelength range. Thus the LP_{01}-LP_{03} mode interference spectrum shows a series of quite uniform fringes in Fig. 4.2(f).

4.3 Mode discrimination in transmission spectra

Figure 4.3 shows a transmission spectrum of the HOMF modal interferometer with a 1-meter HOMF obtained by launching light from a broadband light source to an optical spectrum analyzer (86142A, Agilent). Modal behaviors of the LP_{01}-LP_{02} modes allow a high-visibility interference pattern where the critical wavelength locates at 1559.4 nm that coincides well with the simulated one in Fig. 4.2(e) with 3nm error. Furthermore, the inset of Fig. 4.3 shows that there exists a noticeable amplitude modulation in a low-contrast interference fringe due to the presence of less intense mode interference between the LP_{01} and LP_{03} modes.

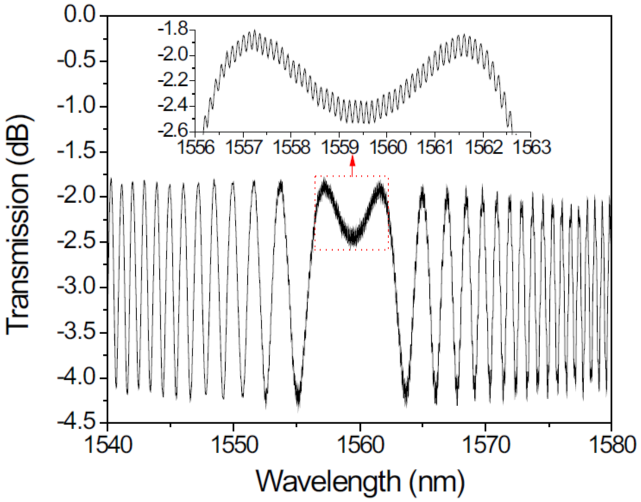

Figure 4.3 Transmission spectrum of the 1-meter HOMF modal interferometer, inset: An enlargement around the critical wavelength of 1559.4 nm.

To further investigate the dispersion characteristics of mode interference in a HOMF, a power spectrum in the spatial frequency domain is obtained and shown in Fig. 4.4 by performing a Fourier Transform on the transmission spectrum in the wavelength domain in Fig. 4.3. The spatial frequency $\xi(\lambda)$ can be written as $\xi_{2(3)}(\lambda) = 1/\Delta\lambda \approx \Delta n_{2(3)}(\lambda)L/\lambda_0^2$, where $\Delta\lambda$ is the wavelength spacing between two neighboring peaks of the interference spectrum, λ_0 is the center peak wavelength around which a Taylor series is expanded [59].. Fig. 4.4 and its inset exhibit two separate clusters of multiple peaks in the spatial frequency domain that correspond to two orders of core mode coupling with significant chromatic dispersion effects within the wavelength range from 1540 nm to 1580 nm. One dominant group of peaks ranges from 0 - 2 nm^{-1} that corresponds to the LP$_{01}$-LP$_{02}$ mode coupling. The other group of peaks extends a spatial frequency range from 6 - 10 nm^{-1}, which corresponds to the LP$_{01}$-LP$_{03}$ mode coupling.

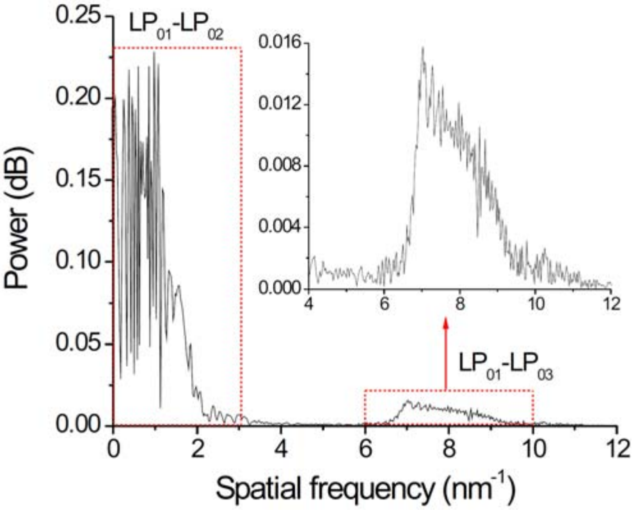

Figure 4.4 Power spectrum in the spatial frequency domain of the 1-meter HOMF modal interferometer, inset: The group of peaks corresponding to the LP01-LP03 mode coupling.

Alternatively, the 1-meter HOMF was replaced by a 1-centimeter HOMF in the SMF-HOMF-SMF structure to measure and discriminate temperature and axial strain effects in a more compact way. Since the peak wavelength spacing is inversely proportional to the length of the HOMF, the amplitude modulation in the interference fringes of the 1-centimeter HOMF modal interferometer as shown in the inset of Fig. 4.5(a) is due to the LP$_{01}$-LP$_{03}$ mode coupling while the interference fringe envelope is caused by the LP$_{01}$-LP$_{02}$ mode coupling. Figure 4.5(a) shows the power spectrum of the 1-centimeter HOMF modal interferometer in the spatial frequency domain, where a dominant peak for the LP$_{02}$ mode locates at 0.0222 nm^{-1}, and other three lower peaks for the LP$_{03\text{-}1}$, LP$_{03\text{-}2}$, and LP$_{03\text{-}3}$ modes locate at 0.0444 nm^{-1}, 0.0888 nm^{-1}, and 0.1222 nm^{-1}, respectively. Compared with the 1-meter HOMF modal interferometer, less dispersion information is carried in the 1-centimeter one even for a larger wavelength span because the spatial frequency is proportional to the length of the HOMF. Figure 4.5(b) shows a phase spectrum in the spatial frequency domain where the normalized phase in the range of 0 and 2π were obtained from the Fourier transformed data at each spatial frequency.

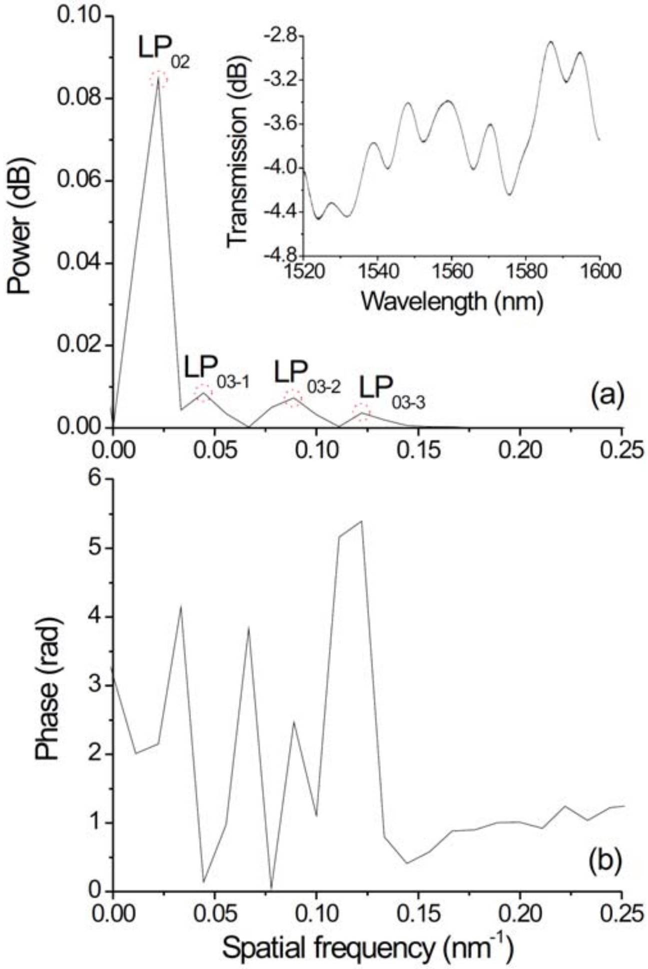

Figure 4.5 The 1-centimeter HOMF modal interferometer: (a) Power spectrum in the spatial frequency domain, inset: Transmission spectrum in the wavelength domain; (b) Phase spectrum in the spatial frequency domain.

4.4 Operation principle and experimental results

The shift in the phase difference between the LP_{01} mode and the LP_{02} or LP_{03} mode, $\delta(\Delta\Phi_{\mathrm{T},\varepsilon})$, at a particular spatial frequency can be expressed by

$$\delta(\Delta\Phi_{\mathrm{T}(\varepsilon)}) = -2\pi\xi\delta\lambda_{\mathrm{T}(\varepsilon)}, \tag{4.4}$$

where $\delta\lambda_{\mathrm{T},\varepsilon}$ is the temperature or axial strain induced peak wavelength shift in the interference spectrum between the LP_{01} mode and the LP_{02} or LP_{03} mode. In Fig. 4.5(a), the unique peak with highest intensity corresponds to the LP_{01}-LP_{02} mode coupling in a large spectral range, which may exhibit cross-talk on chromatic dispersion and poor linearity under changes in temperature and axial strain. Thus the group of three peaks originating from strong dispersion effects of the LP_{01}-LP_{03} modes is utilized for temperature-strain discrimination because of their different responses in modal effective indices under an equal disturbance variance condition. It is noted that the phase shift is negatively proportional to the corresponding interference peak wavelength shift, $\delta\lambda$, which is given by

$$\delta\lambda_{\mathrm{T}(\varepsilon)} = \left(\frac{\delta L_{\mathrm{T}(\varepsilon)}}{L} + \frac{\delta\left(\Delta n_{\mathrm{T}(\varepsilon)}\right)}{\Delta n} \right)\lambda, \tag{4.5}$$

where $\delta L_{\mathrm{T}(\varepsilon)}$ and $\delta(\Delta n_{\mathrm{T}(\varepsilon)})$ are changes in the length of the HOMF and the difference in the modal effective indices. Both the fiber length and the difference in the modal effective indices will increase due to the thermo-elastic and thermo-optic effects with an increasing temperature. Therefore the phase difference of the HOMF modal interferometer will experience blue-shift according to Eqs. (4.4) and (4.5). When the axial strain is applied on the HOMF modal interferometer, the fiber will be stretched, and the difference in the modal effective indices is contributed by both the fiber geometry modification and the photo-elastic effect which makes the positive and negative sign of $\delta(\Delta n_{\varepsilon})$ both possible. Thus the phase difference will experience either blueshift or redshift, depending upon the relative magnitudes of $\delta L/L$ and $\delta(\Delta n_{\varepsilon})/\Delta n_{\varepsilon}$. Figure 4.6 shows experimental results of temperature and axial strain dependences of the phase difference at different spatial frequencies corresponding to distinct chromatic dispersion effects of the LP_{01}-LP_{03} modes. As shown in Fig. 4.6(a), the temperature coefficients of the $LP_{03\text{-}1}$, $LP_{03\text{-}2}$, and $LP_{03\text{-}3}$ modes are -0.0353±0.0007 rad/°C, -0.0307±0.0004 rad/°C, and -0.019±0.001 rad/°C, respectively. As shown in Fig. 4.6(b), the axial strain coefficients of the $LP_{03\text{-}1}$, $LP_{03\text{-}2}$, and $LP_{03\text{-}3}$ modes are -454±14 rad/ε, -88±3 rad/ε, and 85±6 rad/ε, respectively. Each mode has a distinctive sensitivity to both temperature and axial strain, which effectively enables simultaneous measurement of multi-parameters.

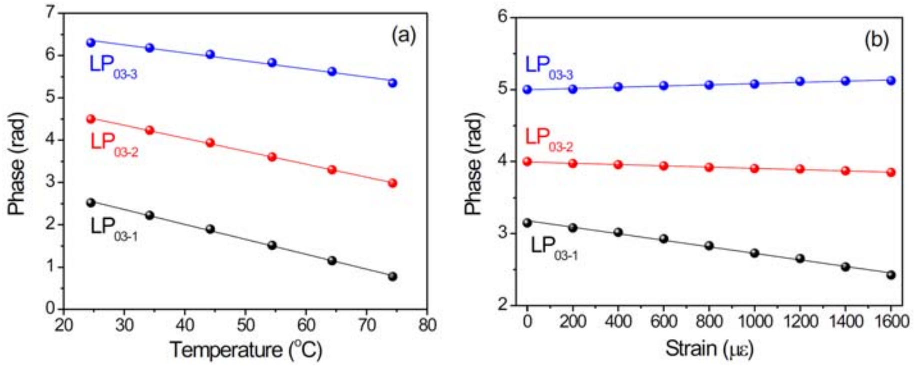

Figure 4.6 Experimental results of phase versus (a) temperature and (b) axial strain at different spatial frequencies.

A character matrix $M^{m}_{T,\varepsilon}$ is defined to represent the sensing performance of the mth order LP0m modes in the HOMF modal fiber interferometer by

$$\begin{bmatrix} \delta\Phi_{0\text{m-i}} \\ \delta\Phi_{0\text{m-i'}} \end{bmatrix} = M^{\text{m}}_{T,\varepsilon} \begin{bmatrix} \Delta \text{T} \\ \Delta\varepsilon \end{bmatrix} = \begin{bmatrix} C^{\text{T}}_{0\text{m-i}} & C^{\varepsilon}_{0\text{m-i}} \\ C^{\text{T}}_{0\text{m-i'}} & C^{\varepsilon}_{0\text{m-i'}} \end{bmatrix} \begin{bmatrix} \Delta \text{T} \\ \Delta\varepsilon \end{bmatrix}, \tag{4.6}$$

where i and i' represent two arbitrary selected LP0m-i modes for the temperature and axial strain discrimination. $C_{03\text{-}i}^{T}$, $C_{03\text{-}i'}^{T}$, $C_{03\text{-}i}^{\varepsilon}$, and $C_{03\text{-}i'}^{\varepsilon}$ are the temperature and axial strain coefficients of the

$LP_{03\text{-i}}$ mode and the $LP_{03\text{-i}'}$ mode, respectively. According to the error analysis for the simultaneous measurement of multiple parameters given by

$$\begin{aligned} \delta T &= \frac{\left|C^{\varepsilon}_{03\text{-i}}\right| \delta\Phi_{03\text{-i}} + \left|C^{\varepsilon}_{03\text{-i}'}\right| \delta\Phi_{03\text{-i}'}}{\left|C^{T}_{03\text{-i}} C^{\varepsilon}_{03\text{-i}'} - C^{\varepsilon}_{03\text{-i}} C^{T}_{03\text{-i}'}\right|}, \\ \delta\varepsilon &= \frac{\left|C^{T}_{03\text{-i}}\right| \delta\Phi_{03\text{-i}} + \left|C^{T}_{03\text{-i}'}\right| \delta\Phi_{03\text{-i}'}}{\left|C^{T}_{03\text{-i}} C^{\varepsilon}_{03\text{-i}'} - C^{\varepsilon}_{03\text{-i}} C^{T}_{03\text{-i}'}\right|}. \end{aligned} \tag{4.7}$$

The minimum errors of temperature and axial strain are calculated to be 0.15 ^{o}C and 22 με, 0.15 ^{o}C and 19 με, and 0.24 ^{o}C and 68 με, for the mode coupling between LP_{01} and $LP_{03\text{-}1}$, $LP_{03\text{-}2}$, $LP_{03\text{-}3}$, respectively.

4.5 Conclusion

In conclusion, an approach employing the joint effect of chromatic dispersion and intermodal dispersion of SMF-HOMF-SMF structure to fulfill dual-parameter measurements is proposed. A new scheme based on fast Fourier transform algorithm is applied to analyze the mode coupling and discriminate the supported modes confined in HOMF. The wavelength dependent dispersion leads to the multiple peaks in the spatial frequency domain, which provides the availability of abundant choices of sensitivities to the environmental disturbances. By appropriately making options on the length of central HOMF part according to the practical need, this easy-fabricating and compact sensing structure would be potentially applicable in situation where more than two parameters are required to be discriminated.

4.6 Comparison with tapered BIF-MZI

Previously, tapered BIF-MZI has been successfully utilized to discriminate the temperature and refractive index based on the phase demodulation scheme. This kind of structure is also potentially capable of realizing the simultaneous temperature and strain measurements as shown in this chapter. The reason why HOMF is chosen in this work instead of tapered BIF-MZI is because HOMF can support the same types of three stable core modes even the device is stretched under strain or heated by increasing temperature, which guarantees a reliable and repeatable measurement within a large temperature or strain range. However this is not the case for the tapered BIF-MZI where the cladding modes are excited with different types when the device is under different strain due to the deformation of the taper region. Furthermore, because of the strong dispersion effect, the HOMF structure has a higher sensitivity than tapered BIF-MZI for the sensing as long as larger spatial frequency peaks which correspond to positions beyond the critical wavelength are selected for discrimination. The measurement errors could be controlled to a small value by choosing the peaks with distinct phase responses.

Chapter 5

Summary and future work

5.1 Summary

In this dissertation, two novel kinds of in-line fiber Mach-Zehnder interferometers are proposed for vibration sensing and discrimination of temperature and strain, respectively. Compared to other types of optical fiber sensors previously investigated, the in-line fiber MZI presents more fascinating and attractive advantages, such as easy fabrication, potential low cost, light weight, high integrity, simple packaging and so on.

The tapered bend-insensitive fiber Mach-Zehnder interferometer is the first in-line fiber MZI structure for vibration measurements. This interferometer is manufactured without removing the central protective jacket between the two tapers, which significantly increases the mechanical strength of the sensor, protects the device from external physical damage and provides easy attachment to the vibrating source. Besides these benefits, the remaining of coating also guarantees the cladding modes that are interfering with core mode are only inner-type with quite limited number. The limited number of inner-cladding modes leads to a quite uniform transmission spectral profile and makes sure a uniform sinusoid response to vibration. The high sensitive and fast intensity demodulation scheme is employed by monitoring the power fluctuation at a selected wavelength to recover the frequencies of different vibrations. An extremely wide range of frequency responses from 1 Hz up to 500 kHz with high SNR is realized by employing the proposed BIF-MZI, which demonstrates that this device would be an excellent alternative for intrusion detection and structure health monitoring.

The chromatic dispersion and intermodal dispersion effects in SMF-HOMF-SMF are analyzed in detail and simulated for each supported core mode. The multi-peak feature induced by the dispersion effect provides abundant sensitivity choices for multi-parameter sensing. The phase demodulation scheme is utilized for extracting and monitoring the phase shift of the selected peaks in the spatial frequency domain. Since the phases of spatial frequency peaks have different temperature and strain dependences, by appropriately making options on the length of the central HOMF part and peak positions, dual-parameter or even more parameters could be simultaneously measured. This easy fabricating and compact device could be potentially applicable in wide areas where the cross-sensitivity problem should be resolved.

5.2 Future work

Since we have proposed a highly sensitive in-line fiber sensor for measuring the mechanical vibration, the acoustic wave detection would be potentially realized by using the similar kinds of devices which are probably required with higher sensitivity. This would be a promising future research on fiber sensors that can replace the conventional piezoceramic sensors in electromagnetic sensitive environments.

By exciting leaky modes of the microstructured fiber sensors, a highly sensitive temperature sensor can be realized. This would lead to some applications where measurements of temperature with high resolution are needed.

Combining the micro-fiber structure with Brillouin effects studies is another promising orientation. The Brillouin cooling effect is just observed in a gentle fiber taper structure and a lot of more work should be performed for further investigation.

Bibliography

[1] M. F. G. K. A. Murphy, A. Wang, R. O. Claus, and A. M. Vengsarkar, A. M., "Extrinsic Fabry Perot optical fiber sensor," ***Eighth Optical Fiber Sensors Conference***, 193–196 (1992).

[2] Z. L. Ran, Y. J. Rao, W. J. Liu, X. Liao, and K. S. Chiang, "Laser-micromachined Fabry-Perot optical fiber tip sensor for high-resolution temperature-independent measurement of refractive index," ***Opt Express*** **16**, 2252-2263 (2008).

[3] T. W. Kao and H. F. Taylor, "High-sensitivity intrinsic fiber-optic Fabry-Perot pressure sensor," ***Opt Lett*** **21**, 615-617 (1996).

[4] T. Wei, Y. K. Han, H. L. Tsai, and H. Xiao, "Miniaturized fiber inline Fabry-Perot interferometer fabricated with a femtosecond laser," ***Opt Lett*** **33**, 536-538 (2008).

[5] Y. Li, X. Z. Wang, and X. Y. Bao, "Sensitive acoustic vibration sensor using single-mode fiber tapers," ***Appl Optics*** **50**, 1873-1878 (2011).

[6] T. C. Li, A. Wang, K. Murphy, and R. Claus, "White-Light Scanning Fiber Michelson Interferometer for Absolute Position-Distance Measurement," ***Opt Lett*** **20**, 785-787 (1995).

[7] Z. B. Tian, S. S. H. Yam, and H. P. Loock, "Refractive index sensor based on an abrupt taper Michelson interferometer in a single-mode fiber," ***Opt Lett*** **33**, 1105-1107 (2008).

[8] Z. B. Tian, S. S. H. Yam, and H. P. Loock, "Single-mode fiber refractive index sensor based on core-offset attenuators," ***IEEE Photonic Tech L*** **20**, 1387-1389 (2008).

[9] X. Y. Dong, H. Y. Tam, and P. Shum, "Temperature-insensitive strain sensor with polarization-maintaining photonic crystal fiber based Sagnac interferometer," ***Appl Phys Lett*** **90**(2007).

[10] A. N. Starodumov, L. A. Zenteno, D. Monzon, and E. DeLaRosa, "Fiber Sagnac interferometer temperature sensor," ***Appl Phys Lett*** **70**, 19-21 (1997).

[11] M. G. Xu, J. L. Archambault, L. Reekie, and J. P. Dakin, "Discrimination between Strain and Temperature Effects Using Dual-Wavelength Fiber Grating Sensors," ***Electron Lett*** **30**, 1085-1087 (1994).

[12] P. C. Hill and B. J. Eggleton, "Strain Gradient Chirp of Fiber Bragg Gratings," ***Electron Lett*** **30**, 1172-1174 (1994).

[13] V. Bhatia and A. M. Vengsarkar, "Optical fiber long-period grating sensors," ***Opt Lett* 21**, 692-694 (1996).

[14] S. W. James, M. L. Dockney, and R. P. Tatam, "Simultaneous independent temperature and strain measurement using in-fibre Bragg grating sensors," ***Electron Lett* 32**, 1133-1134 (1996).

[15] X. W. Shu, Y. Liu, D. H. Zhao, B. Gwandu, F. Floreani, L. Zhang, and I. Bennion, "Dependence of temperature and strain coefficients on fiber grating type and its application to simultaneous temperature and strain measurement," ***Opt Lett* 27**, 701-703 (2002).

[16] B. O. Guan, H. Y. Tam, H. L. W. Chan, C. L. Choy, and M. S. Demokan, "Discrimination between strain and temperature with a single fiber Bragg grating," ***Microw Opt Techn Let* 33**, 200-202 (2002).

[17] V. Bhatia, D. Campbell, R. O. Claus, and A. M. Vengsarkar, "Simultaneous strain and temperature measurement with long-period gratings," ***Opt Lett* 22**, 648-650 (1997).

[18] K. J. Han, Y. W. Lee, J. Kwon, S. Roh, J. Jung, and B. Lee, "Simultaneous measurement of strain and temperature incorporating a long-period fiber grating inscribed on a polarization-maintaining fiber," ***IEEE Photonic Tech L* 16**, 2114-2116 (2004).

[19] G. Y. Sun, D. S. Moon, and Y. Chung, "Simultaneous temperature and strain measurement using two types of high-birefringence fibers in Sagnac loop mirror," ***IEEE Photonic Tech L* 19**, 2027-2029 (2007).

[20] A. M. Vengsarkar, W. C. Michie, L. Jankovic, B. Culshaw, and R. O. Claus, "Fiberoptic Dual-Technique Sensor for Simultaneous Measurement of Strain and Temperature," ***J Lightwave Technol* 12**, 170-177 (1994).

[21] C. R. F. S. W. Doebling, M. B. Prime, and D. W. Shevitz, "Damage Identification and Health Monitoring of Structural and Mechanical Systems from Changes in Their Vibration Characteristics: A Literature Review," ***Los Alamos National Laboratory, Tech. Rep. LA-13070-MS*** (1996).

[22] W. J. Zhou, X. Y. Dong, K. Ni, C. C. Chan, and P. Shum, "Temperature-insensitive accelerometer based on a strain-chirped FBG," ***Sensor Actuat a-Phys* 157**, 15-18 (2010).

[23] T. A. Guo, A. C. L. Wong, W. S. Liu, B. O. Guan, C. Lu, and H. Y. Tam, "Beat-frequency adjustable Er3+-doped DBR fiber laser for ultrasound detection," ***Opt Express* 19**, 2485-2492 (2011).

[24] A. Leung, P. M. Shankar, and R. Mutharasan, "A review of fiber-optic biosensors," ***Sensor Actuat B-Chem* 125**, 688-703 (2007).

[25] L. Wen-xu and C. Jian, "Continuous monitoring of adriamycin in vivo using fiber optic-based fluorescence chemical sensor," ***Anal Chem*** **75**, 1458-1462 (2003).

[26] G. P. Anderson, J. P. Golden, and F. S. Ligler, "A Fiber Optic Biosensor - Combination Tapered Fibers Designed for Improved Signal Acquisition," ***Biosens Bioelectron*** **8**, 249-256 (1993).

[27] A. J. C. Tubb, F. P. Payne, R. B. Millington, and C. R. Lowe, "Single-mode optical fibre surface plasma wave chemical sensor," ***Sensor Actuat B-Chem*** **41**, 71-79 (1997).

[28] J. F. Masson, L. Obando, S. Beaudoin, and K. Booksh, "Sensitive and real-time fiber-optic-based surface plasmon resonance sensors for myoglobin and cardiac troponin I," ***Talanta*** **62**, 865-870 (2004).

[29] K. Bohnert, P. Gabus, J. Nehring, and H. Brandle, "Temperature and vibration insensitive fiber-optic current sensor," ***J Lightwave Technol*** **20**, 267-276 (2002).

[30] D. S. W. Y. X. Niu, Y. F.Wang, C. Zhang, and P. Zhang, "Faraday optical fiber current sensor with phase conjugate device," ***Proc. SPIE 4920***, 400–404 (2002).

[31] Y. W. Lee, Y. Yoon, and B. Lee, "A simple fiber-optic current sensor using a long-period fiber grating inscribed on a polarization-maintaining fiber as a sensor demodulator," ***Sensor Actuat a-Phys*** **112**, 308-312 (2004).

[32] K. Bohnert, H. Brandle, M. G. Brunzel, P. Gabus, and P. Guggenbach, "Highly accurate fiber-optic DC current sensor for the electrowinning industry," ***IEEE T Ind Appl*** **43**, 180-187 (2007).

[33] K. Bohnert, P. Gabus, J. Nehring, H. Brandle, and M. G. Brunzel, "Fiber-optic current sensor for electrowinning of metals," ***J Lightwave Technol*** **25**, 3602-3609 (2007).

[34] M. Belal, Z. Song, Y. Jung, G. Brambilla, and T. P. Newson, "Optical fiber microwire current sensor," ***Opt Lett*** **35**, 3045-3047 (2010).

[35] W. W. Lin, "Fiber-optic current sensor," ***Opt Eng*** **42**, 896-897 (2003).

[36] M. Belal, Z. Q. Song, Y. M. Jung, G. Brambilla, and T. P. Newson, "An interferometric current sensor based on optical fiber micro wires," ***Opt Express*** **18**, 19951-19956 (2010).

[37] L. Jiang, L. J. Zhao, S. M. Wang, J. P. Yang, and H. Xiao, "Femtosecond laser fabricated all-optical fiber sensors with ultrahigh refractive index sensitivity: modeling and experiment," ***Opt Express*** **19**, 17591-17598 (2011).

[38] D. W. Duan, Y. J. Rao, L. C. Xu, T. Zhu, D. Wu, and J. Yao, "In-fiber Mach-Zehnder

interferometer formed by large lateral offset fusion splicing for gases refractive index measurement with high sensitivity," ***Sensor Actuat B-Chem*** **160**, 1198-1202 (2011).

[39] H. J. Patrick, C. C. Chang, and S. T. Vohra, "Long period fibre gratings for structural bend sensing," ***Electron Lett*** **34**, 1773-1775 (1998).

[40] Y. Liu, L. Zhang, J. A. R. Williams, and I. Bennion, "Optical bend sensor based on measurement of resonance mode splitting of long-period fiber grating," ***IEEE Photonic Tech L*** **12**, 531-533 (2000).

[41] H. P. Gong, C. C. Chan, P. Zu, L. H. Chen, and X. Y. Dong, "Curvature measurement by using low-birefringence photonic crystal fiber based Sagnac loop," ***Opt Commun*** **283**, 3142-3144 (2010).

[42] Y. Jeong, S. Baek, Y. Lee, S. Choi, and K. Oh, "Macrobend sensor via the use of a hollow-core splice fiber: theory and experiments," ***Opt Eng*** **41**, 1815-1820 (2002).

[43] W. Jin, H. F. Xuan, and H. L. Ho, "Sensing with hollow-core photonic bandgap fibers," ***Meas Sci Technol*** **21**(2010).

[44] W. Shin, Y. L. Lee, B. A. Yu, Y. C. Noh, and T. J. Ahn, "Highly sensitive strain and bending sensor based on in-line fiber Mach-Zehnder interferometer in solid core large mode area photonic crystal fiber," ***Opt Commun*** **283**, 2097-2101 (2010).

[45] M. Deng, C. P. Tang, T. Zhu, and Y. J. Rao, "Highly sensitive bend sensor based on Mach-Zehnder interferometer using photonic crystal fiber," ***Opt Commun*** **284**, 2849-2853 (2011).

[46] D. Sagrario and P. Mead, "Axial and angular displacement fiber-optic sensor," ***Appl Optics*** **37**, 6748-6754 (1998).

[47] X. Y. Dong, Y. Q. Liu, Z. G. Liu, and X. Y. Dong, "Simultaneous displacement and temperature measurement with cantilever-based fiber Bragg grating sensor," ***Opt Commun*** **192**, 213-217 (2001).

[48] A. Mehta, W. Mohammed, and E. G. Johnson, "Multimode interference-based fiber-optic displacement sensor," ***IEEE Photonic Tech L*** **15**, 1129-1131 (2003).

[49] A. Yariv, "Optical Electronics in modern communications," ***Oxford University Press*** (1997).

[50] C. Tsao, "Optical Fiber Waveguide Analysis," ***Oxford University Press*** (1992).

[51] R. J. Black and R. Bourbonnais, "Core-Mode Cutoff for Finite-Cladding Lightguides," ***Iee Proc-J*** **133**, 377-384 (1986).

[52] Z. B. Tian and S. S. H. Yam, "In-Line Abrupt Taper Optical Fiber Mach-Zehnder

Interferometric Strain Sensor," ***IEEE Photonic Tech L*** **21**, 161-163 (2009).

[53] P. Lu, L. Q. Men, K. Sooley, and Q. Y. Chen, "Tapered fiber Mach-Zehnder interferometer for simultaneous measurement of refractive index and temperature," ***Appl Phys Lett*** **94**(2009).

[54] T. Chen, R. Chen, P. Lu, Q. Chen, and K. P. Chen, "Tapered fibre Mach-Zehnder interferometer for simultaneous measurement of liquid level and temperature," ***Electron Lett*** **47**, 1093-1094 (2011).

[55] P. Lu, G. B. Lin, X. Z. Wang, L. Chen, and X. Y. Bao, "Lateral Stress Detection Using a Tapered Fiber Mach-Zehnder Interferometer," ***IEEE Photonic Tech L*** **24**, 2038-2041 (2012).

[56] Q. Wang, G. Farrell, and W. Yan, "Investigation on single-mode-multimode single-mode fiber structure," ***J Lightwave Technol*** **26**, 512-519 (2008).

[57] S. M. Tripathi, A. Kumar, R. K. Varshney, Y. B. P. Kumar, E. Marin, and J. P. Meunier, "Strain and Temperature Sensing Characteristics of Single-Mode-Multimode-Single-Mode Structures," ***J Lightwave Technol*** **27**, 2348-2356 (2009).

[58] E. Salik, M. Medrano, G. Cohoon, J. Miller, C. Boyter, and J. Koh, "SMS Fiber Sensor Utilizing a Few-Mode Fiber Exhibits Critical Wavelength Behavior," ***IEEE Photonic Tech L*** **24**, 593-595 (2012).

[59] H. Y. Choi, M. J. Kim, and B. H. Lee, "All-fiber Mach-Zehnder type interferometers formed in photonic crystal fiber," ***Opt Express*** **15**, 5711-5720 (2007).

[60] D. W. Duan, Y. J. Rao, L. C. Xu, T. Zhu, M. Deng, D. Wu, and J. Yao, "In-Fiber Fabry-Perot and Mach-Zehnder interferometers based on hollow optical fiber fabricated by arc fusion splicing with small lateral offsets," ***Opt Commun*** **284**, 5311-5314 (2011).

[61] S. W. James and R. P. Tatam, "Optical fibre long-period grating sensors: Characteristics and application," ***Meas Sci Technol*** **14**, R49-R61 (2003).

[62] B. H. Lee and J. Nishii, "Dependence of fringe spacing on the grating separation in a long-period fiber grating pair," ***Appl Optics*** **38**, 3450-3459 (1999).

[63] S. K. A. K. Bey, T. Sun, and K. T. V. Grattan, "Optimization of a long-period grating-based Mach-Zehnder interferometer for temperature measurement," ***Opt Commun*** **272**, 15-21 (2007).

[64] O. Duhem, J. F. Henninot, and M. Douay, "Study of in fiber Mach-Zehnder interferometer based on two spaced 3-dB long period gratings surrounded by a refractive index higher than that of silica," ***Opt Commun*** **180**, 255-262 (2000).

[65] Y. J. Kim, U. C. Paek, and B. H. Lee, "Measurement of refractive-index variation with temperature by use of long-period fiber gratings," ***Opt Lett*** **27**, 1297-1299 (2002).

[66] J. F. Ding, A. P. Zhang, L. Y. Shao, J. H. Yan, and S. L. He, "Fiber-taper seeded long-period grating pair as a highly sensitive refractive-index sensor," ***IEEE Photonic Tech L*** **17**, 1247-1249 (2005).

[67] J. H. Lim, H. S. Jang, K. S. Lee, J. C. Kim, and B. H. Lee, "Mach-Zehnder interferometer formed in a photonic crystal fiber based on a pair of long-period fiber gratings," ***Opt Lett*** **29**, 346-348 (2004).

[68] K. M. Davis, K. Miura, N. Sugimoto, and K. Hirao, "Writing waveguides in glass with a femtosecond laser," ***Opt Lett*** **21**, 1729-1731 (1996).

[69] A. Martinez, M. Dubov, I. Khrushchev, and I. Bennion, "Direct writing of fibre Bragg gratings by femtosecond laser," ***Electron Lett*** **40**, 1170-1172 (2004).

[70] A. M. Streltsov and N. F. Borrelli, "Fabrication and analysis of a directional coupler written in glass by nanojoule femtosecond laser pulses," ***Opt Lett*** **26**, 42-43 (2001).

[71] Y. Cheng, H. L. Tsai, K. Sugioka, and K. Midorikawa, "Fabrication of 3D microoptical lenses in photosensitive glass using femtosecond laser micromachining," ***Appl Phys a-Mater*** **85**, 11-14 (2006).

[72] Y. Cheng, K. Sugioka, and K. Midorikawa, "Microfluidic laser embedded in glass by three-dimensional femtosecond laser microprocessing," ***Opt Lett*** **29**, 2007-2009 (2004).

[73] H. Y. Zheng, H. Liu, S. Wan, G. C. Lim, S. Nikumb, and Q. Chen, "Ultrashort pulse laser micromachined microchannels and their application in an optical switch," ***Int J Adv Manuf Tech*** **27**, 925-929 (2006).

[74] L. J. Zhao, L. Jiang, S. M. Wang, H. Xiao, Y. F. Lu, and H. L. Tsai, "A High-Quality Mach-Zehnder Interferometer Fiber Sensor by Femtosecond Laser One-Step Processing," ***Sensors-Basel*** **11**, 54-61 (2011).

[75] T. Wei, X. W. Lan, and H. Xiao, "Fiber Inline Core-Cladding-Mode Mach-Zehnder Interferometer Fabricated by Two-Point CO2 Laser Irradiations," ***IEEE Photonic Tech L*** **21**, 669-671 (2009).

[76] O. Frazao, J. Viegas, P. Caldas, J. L. Santos, F. M. Araujo, L. A. Ferreira, and F. Farahi, "All-fiber Mach-Zehnder curvature sensor based on multimode interference combined with a long-period grating," ***Opt Lett*** **32**, 3074-3076 (2007).

[77] O. Frazao, R. Falate, J. L. Fabris, J. L. Santos, L. A. Ferreira, and F. M. Araujo, "Optical inclinometer based on a single long-period fiber grating combined with a

fused taper," ***Opt Lett*** **31**, 2960-2962 (2006).

[78] P. Lu and Q. Y. Chen, "Femtosecond laser microfabricated fiber Mach-Zehnder interferometer for sensing applications," ***Opt Lett*** **36**, 268-270 (2011).

[79] X. Y. Dong, L. Su, P. Shum, Y. Chung, and C. C. Chan, "Wavelength-selective all-fiber filter based on a single long-period fiber grating and a misaligned splicing point," ***Opt Commun*** **258**, 159-163 (2006).

[80] P. Lu and Q. Y. Chen, "Asymmetrical Fiber Mach-Zehnder Interferometer for Simultaneous Measurement of Axial Strain and Temperature," ***IEEE Photonics J*** **2**, 942-953 (2010).

[81] T. Guo, A. Ivanov, C. K. Chen, and J. Albert, "Temperature-independent tilted fiber grating vibration sensor based on cladding-core recoupling," ***Opt Lett*** **33**, 1004-1006 (2008).

[82] A. Wada, S. Tanaka, and N. Takahashi, "Optical Fiber Vibration Sensor Using FBG Fabry-Perot Interferometer With Wavelength Scanning and Fourier Analysis," ***IEEE Sens J*** **12**, 225-229 (2012).

[83] B. Lee, "Review of the present status of optical fiber sensors," ***Opt Fiber Technol*** **9**, 57-79 (2003).

[84] F. F. Pang, W. C. Xiang, H. R. Guo, N. Chen, X. L. Zeng, Z. Y. Chen, and T. Y. Wang, "Special optical fiber for temperature sensing based on cladding-mode resonance," ***Opt Express*** **16**, 12967-12972 (2008).

[85] F. F. Pang, W. B. Liang, W. C. Xiang, N. Chen, X. L. Zeng, Z. Y. Chen, and T. Y. Wang, "Temperature-Insensitivity Bending Sensor Based on Cladding-Mode Resonance of Special Optical Fiber," ***IEEE Photonic Tech L*** **21**, 76-78 (2009).

[86] Y. Wang, M. W. Yang, D. N. Wang, S. J. Liu, and P. X. Lu, "Fiber in-line Mach-Zehnder interferometer fabricated by femtosecond laser micromachining for refractive index measurement with high sensitivity," ***J Opt Soc Am B*** **27**, 370-374 (2010).

[87] H. H. Liu, F. F. Pang, H. R. Guo, W. X. Cao, Y. Q. Liu, N. Chen, Z. Y. Chen, and T. Y. Wang, "In-series double cladding fibers for simultaneous refractive index and temperature measurement," ***Opt Express*** **18**, 13072-13082 (2010).

[88] F. F. Pang, H. H. Liu, H. R. Guo, Y. Q. Liu, X. L. Zeng, N. Chen, Z. Y. Chen, and T. Y. Wang, "In-Fiber Mach-Zehnder Interferometer Based on Double Cladding Fibers for Refractive Index Sensor," ***IEEE Sens J*** **11**, 2395-2400 (2011).

[89] R. M. Gerosa, D. H. Spadoti, L. D. Menezes, and C. J. S. de Matos, "In-fiber modal Mach-Zehnder interferometer based on the locally post-processed core of a photonic

crystal fiber," ***Opt Express*** **19**, 3124-3129 (2011).

[90] C. Y. Shen, C. Zhong, Y. You, J. L. Chu, X. Zou, X. Y. Dong, Y. X. Jin, J. F. Wang, and H. P. Gong, "Polarization-dependent curvature sensor based on an in-fiber Mach-Zehnder interferometer with a difference arithmetic demodulation method," ***Opt Express*** **20**, 15406-15417 (2012).

[91] L. C. Li, L. Xia, Z. H. Xie, and D. M. Liu, "All-fiber Mach-Zehnder interferometers for sensing applications," ***Opt Express*** **20**, 11109-11120 (2012).

[92] J. H. Wo, G. H. Wang, Y. Cui, Q. Z. Sun, R. B. Liang, P. P. Shum, and D. M. Liu, "Refractive index sensor using microfiber-based Mach-Zehnder interferometer," ***Opt Lett*** **37**, 67-69 (2012).

[93] K. Nakajima, K. Hogari, T. Zhou, K. Tajima, and I. Sankawa, "Hole-assisted fiber design for small bending and splice losses," ***IEEE Photonic Tech L*** **15**, 1737-1739 (2003).

[94] P. R. Watekar, S. Ju, Y. S. Yoon, Y. S. Lee, and W. T. Han, "Design of a trenched bend insensitive single mode optical fiber using spot size definitions," ***Opt Express*** **16**, 13545-13551 (2008).

[95] P. R. Watekar, S. Ju, and W. T. Han, "Design and development of a trenched optical fiber with ultra-low bending loss," ***Opt Express*** **17**, 10350-10363 (2009).

[96] M. J. Li, P. Tandon, D. C. Bookbinder, S. R. Bickham, M. A. McDermott, R. B. Desorcie, D. A. Nolan, J. J. Johnson, K. A. Lewis, and J. J. Englebert, "Ultra-Low Bending Loss Single-Mode Fiber for FTTH," ***J Lightwave Technol*** **27**, 376-382 (2009).

[97] P. R. Watekar, S. Ju, and W. T. Han, "Optimized design of trenched optical fiber for ultralow bending loss at 5 mm of bending diameter," ***Appl Optics*** **50**, E97-E101 (2011).

[98] M. Y. Chen and Y. K. Zhang, "Bend Insensitive Design of Large-Mode-Area Microstructured Optical Fibers," ***J Lightwave Technol*** **29**, 2216-2222 (2011).

[99] D. Boivin, L. A. de Montmorillon, L. Provost, and P. Sillard, "Coherent Multipath Interference in Bend-Insensitive Fibers," ***IEEE Photonic Tech L*** **21**, 1891-1893 (2009).

[100] N. H. Vu, J. T. Kim, E. S. Kim, C. H. Jung, K. G. Lee, and I. K. Hwang, "Ultralow bending loss fibers with higher-order mode strippers," ***Opt Express*** **18**, 19456-19461 (2010).

[101] T. Matsui, K. Nakajima, Y. Goto, T. Shimizu, and T. Kurashima, "Design of Single-Mode and Low-Bending-Loss Hole-Assisted Fiber and Its MPI Characteristics," ***J***

Lightwave Technol **29**, 2499-2505 (2011).

[102] A. Martin, R. Badcock, C. Nightingale, and G. F. Fernando, "A novel optical fiber-based strain sensor," ***IEEE Photonic Tech L*** **9**, 982-984 (1997).

[103] A. H. Gnauck, L. D. Garrett, Y. Danziger, U. Levy, and M. Tur, "Dispersion and dispersion-slope compensation of NZDSF over the entire C band using higher-order-mode fibre," ***Electron Lett*** **36**, 1946-1947 (2000).

[104] S. Ramachandran, S. Ghalmi, S. Chandrasekhar, I. Ryazansky, M. F. Yan, F. V. Dimarcello, W. A. Reed, and P. Wisk, "Tunable dispersion compensators utilizing higher order mode fibers," ***IEEE Photonic Tech L*** **15**, 727-729 (2003).

[105] S. Ramachandran, M. F. Yan, J. Jasapara, P. Wisk, S. Ghalmi, E. Monberg, and F. V. Dimarcello, "High-energy (nanojoule) femtosecond pulse delivery with record dispersion higher-order mode fiber," ***Opt Lett*** **30**, 3225-3227 (2005).

[106] T. J. Chen, "Use of liquid-crystal-clad fiber as a modal filter for a two-mode fiber-optic interferometer," ***Opt Lett*** **29**, 2852-2854 (2004).

[107] L. H. Jae, M. Oh, and Y. D. Kim, "2-Mode Fiberoptic Resonant Ring Interferometer as a Sensor," ***Opt Lett*** **15**, 198-200 (1990).

[108] B. O. Guan, H. Y. Tam, X. M. Tao, and X. Y. Dong, "Simultaneous strain and temperature measurement using a superstructure fiber Bragg grating," ***IEEE Photonic Tech L*** **12**, 675-677 (2000).

[109] H. K. Kang, C. Y. Ryu, C. S. Hong, and C. G. Kim, "Simultaneous measurement of strain and temperature of structures using fiber optic sensor," ***J Intel Mat Syst Str*** **12**, 277-281 (2001).

[110] M. J. Kim, Y. H. Kim, G. Mudhana, and B. H. Lee, "Simultaneous measurement of temperature and strain based on double cladding fiber interferometer assisted by fiber grating pair," ***IEEE Photonic Tech L*** **20**, 1290-1292 (2008).

[111] J. I. Sakai and T. Kimura, "Design of a Miniature Lens for Semiconductor-Laser to Single-Mode Fiber Coupling," ***IEEE J Quantum Elect*** **16**, 1059-1067 (1980).

Curriculum Vitae

Full name	Yanping Xu
Education	M.Sc. (Sep.2011-present) Department of Physics University of Ottawa, Ottawa, Canada Supervisors: Prof. Xiaoyi Bao and Prof. Ping Lu
	B.S. (Sep.2007-Jun.2011) College of Physics Jilin University, Changchun, P. R. China

Publications

Journal Paper

[1] **Yanping Xu**, Ping Lu, Zengguang Qin, Jeremie Harris, Farhana Baset, Ping Lu, Vedula Ravi Bhardwaj, and Xiaoyi Bao, “Vibration sensing using a tapered bend-insensitive fiber based Mach-Zehnder interferometer,” Opt. Express 21(3), 3031-3042 (2013).

[2] P. Lu, J. Harris, **Y. Xu**, Y. Lu, L. Chen, and X. Bao, “Simultaneous refractive index and temperature measurements using a tapered bend-resistant fiber interferometer,” Opt. Lett. 37(22), 4567–4569 (2012).

[3] Jeremie Harris, Ping Lu, Hugo Larocque, **Yanping Xu**, Liang Chen, and Xiaoyi Bao, “Highly sensitive in-fiber interferometric refractometer with temperature and axial strain compensation,” Opt. Express 21(8), 9996-10009 (2013).